Available online at www.sciencedirect.com

SCIENCE DIRECT®

Ore Geology Reviews 29 (2006) 52–76

ORE GEOLOGY REVIEWS

www.elsevier.com/locate/oregeorev

Geology and geochemistry of the Bulong quartz–barite vein-type gold deposit in the Xinjiang Uygur Autonomous Region, China

Fuquan Yang [a,*], Jingwen Mao [a], Yitian Wang [a], Frank P. Bierlein [b]

[a] *Institute of Mineral Resources, Chinese Academy of Geological Sciences, 26 Baiwanzhuang Road, Beijing 100037, People's Republic of China*
[b] *TSRC, School of Earth and Geographical Sciences, University of Western Australia, Crawley, WA 6009, Australia*

Received 27 October 2004; accepted 17 July 2005

Abstract

The Bulong gold deposit, located in Akqi County, Southwest Tianshan, China, occurs in Upper Devonian fine-grained clastic rocks. Gold mineralization is controlled by a series of gently tilted fractured zones. Four ore-bearing quartz–barite veins have been recognized in the Bulong ore district. These range in length from 15 to 660 m and are up to 1 m thick. On the basis of field evidence and petrographic analysis, four stages of vein emplacement and hydrothermal mineralization can be distinguished: (1) an early quartz stage, characterized by the occurrence of massive quartz veins; (2) a barite vein stage; (3) a barite–quartz stage; this represents the main stage of gold mineralization in the Bulong deposit and is characterized by the formation of laminated quartz veins, barite–quartz veins and locally calcite–barite–quartz veins in quartz–barite veins; and (4) a late-stage ankerite–calcite veinlet stage. The ore in these veins occurs as native gold (± pyrite) and is predominantly hosted in quartz and barite.

Two types of fluid inclusions, namely H_2O–NaCl and H_2O–CO_2 ($\pm CH_4/N_2$)–NaCl types, have been recognized in quartz, barite and calcite. Homogenization temperatures of fluid inclusions vary from 159 to 390 °C, with T_h during the main stage of gold mineralization ranging from 200 to 340 °C. Salinity ranges from 2.4 to 46.2 wt.% NaCl equiv. Ore fluid densities range from 0.73 to 1.13 g/cm^3. The $\delta^{34}S$ values of pyrite associated with gold mineralization range from 14.6‰ to 19.2‰ and those of barite from 35.0‰ to 39.6‰, indicating that the sulfur was probably derived from the sedimentary host rocks. The $^3He/^4He$ ratios of fluid inclusions in pyrite are 0.24–0.82 (R/R_a), approximating helium ratios of the crust. The $^{40}Ar/^{36}Ar$ ratios vary from 338 to 471, slightly higher than those indicative of atmospheric argon. The $^{40}Ar/^4He$ ratios of the ore fluids range from 0.02 to 0.41 with a mean of 0.15. Helium and argon isotope compositions of fluid inclusions suggest that the ore fluids of the Bulong gold deposit were mainly derived from the crust. The $\delta^{13}C_{PDB}$ values of fluid inclusions in vein quartz from the Bulong gold deposit define a narrow range of -4.6‰ to -1.4‰. The $\delta^{18}O_{SMOW}$ values of vein quartz range from 17.2‰ to 21.1‰, with corresponding $\delta^{18}O_{fluid}$ values of 6.7‰ to 14.7‰, and δD values of fluid inclusions of between -70‰ and -55‰. The combined isotopic data imply that the ore-forming fluids of the Bulong gold deposit were mainly derived from basinal fluids, with some minor contributions from magmatic fluids and meteoric water, and the carbon in the ore fluids was mainly derived from marine carbonate rocks. The temperature and pressure decrease, local ore-forming fluid boiling, water–rock exchange, changes in composition of ore fluids played important roles in ore-forming processes of the Bulong gold deposit.

Keywords: Quartz–barite vein-type gold mineralization; Fluid inclusions; Stable isotopes; Bulong deposit; China

---

* Corresponding author. Tel.: +86 10 68999075.
E-mail address: fuquanyang@163.com (F. Yang).

0169-1368/$ - see front matter © 2005 Elsevier B.V. All rights reserved.
doi:10.1016/j.oregeorev.2005.07.033

1. Introduction

The Southern Tien Shan Sb–Hg–Au metallogenic belt in Central Asia is one of the important gold belts in the world (Ye et al., 1999; Zheng et al., 2001) and hosts several world-class and superlarge gold deposits, such as the Muruntau gold deposit in Uzbekistan (the world's largest known gold deposit outside the Witwatersrand; Kotov and Poritskaya, 1992; Graupner et al., 2001; Wilde et al., 2001; Yakubchuk et al., 2002), the Kumtor gold deposit in Kyrgyzstan (one of the world's ten largest gold mines; Yakubchuk et al., 2002; Mao et al., 2004), the Jilau gold deposit in Tajikistan (Cole et al., 2000) and the Charmitan gold deposit in Uzbekistan (Bortnikov et al., 1996). The Southwestern Tianshan Mountains in Xinjiang are its eastward extension, with the recently discovered gold deposits at Sawayaerdun, Dashankou, Sahentuohai and Bulong highlighting the exploration potential of this area. The Bulong gold deposit was discovered in the early 1990s and represents a distinct style of gold mineralization that is characterized by a quartz–barite vein association. Gold reserves of the Bulong deposit have been estimated at ca. 1 tonne (No. 8 Geological Party of the Xinjiang Bureau of Geology and Mineral Exploration and Development, 1999), and both gold and barite are currently mined at a small scale. Previously, the Bulong gold deposit has not been studied in great detail. Zheng et al. (1996) carried out a preliminary geochemical study of the host rocks of the deposit. On the basis of a few samples for rare earth elements, trace elements, and stable isotopes studies, Zheng et al. (1996) inferred that ore-forming fluids and solutes were derived from the surrounding host rocks. Yang et al. (1999), Yang and Wu (1999), and Ye et al. (1999) studied the geological characteristics and physico-chemical conditions of the Bulong gold deposit, and proposed that the Bulong deposit displays characteristics of hypabyssal, medium-temperature metallogenesis. Zhao et al. (2002) obtained a Rb–Sr isochron age of 258 ± 15 Ma from fluid inclusions in an auriferous quartz vein.

This paper is the first to describe the metallogenic setting and geological characteristics of this unusual quartz–barite vein-hosted gold deposit and compares it with other types of gold deposits. Systematic fluid inclusion investigations, S, C, O and H stable isotope data and He and Ar isotope data from fluid inclusions are presented. These data form the basis for an assessment of possible sources of the ore-forming fluids and the processes responsible for ore-formation at Bulong.

2. Regional geology

The Bulong gold deposit is situated approx. 45 km SW of Akqi, Kizilsu Kirgiz Autonomous Prefecture, Xinjiang (Fig. 1). Tectonically, the Bulong deposit is located in the Southern Tianshan Hercynian orogenic belt, on the southeastern side of the regional NE-trending Karateki fault, which separates the Late Palaeozoic Southern Tianshan epicontinental basin from the Palaeozoic Kalpin foreland basin (Fig. 1). The basement of the Southwest Tianshan Mountains is Paleo- to Mesoproterozoic in age and composed of gneiss, schist and quartzite. Cambrian rocks exposed in the Kalpin area comprise a suite of neritic limestone intercalated with siltstone and shale, which are overlain by Ordovician limestone, dolomite and fine-grained clastic rocks. Widespread Silurian units are composed of a sequence of carbonate and clastic rocks. The Devonian part of the sequence comprises a sequence of marine carbonate rocks intercalated with clastic rocks, intermediate–basic volcanic rocks, pyroclastic rocks and siliceous

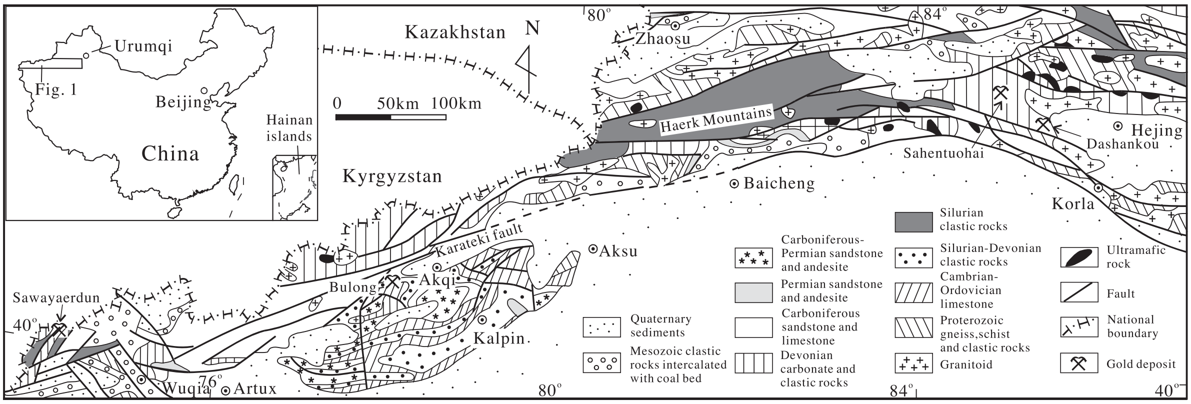

Fig. 1. Simplified regional geological map of the Southwestern Tianshan Mountains in Xinjiang and location of the Bulong gold deposit (modified from Ma, 2002).

rocks, and the Carboniferous units consist of fine-grained clastic rocks with limestone. The Permian units predominantly comprise terrestrial andesite, tuff and terrestrial clastic rocks and the Mesozoic is represented by fluvio-lacustrine clastic rocks with local coal beds and terrestrial volcanic rocks.

Distributed in the vicinity of Baluntai in the northern part of Hejing County, the earliest Proterozoic intrusive rocks in the Southwest Tianshan consist of gneissic quartz diorite and gneissic granodiorite (with a whole-rock Rb–Sr isochron age of 818 Ma; Xinjiang Bureau of Geology and Mineral Exploration and Development, 1993). Devonian–Carboniferous magmatic rocks are abundant and are mainly exposed in the eastern segment of the Southwest Tianshan. The Devonian intrusive rocks belong to the syntectic calc-alkaline series and consist dominantly of monzogranite and K-felspar granite, with subordinate diorite, granodiorite and alkali-feldspar granite and minor mafic–ultramafic rocks and ophiolite (e.g., the Changawuzi ophiolite formed in the Late Silurian–Early Devonian; Cai et al., 1995; Ye et al., 1999). Carboniferous intrusive rocks are composed predominantly of monzogranite with subordinate diorite and granodiorite. Rare Permian post-orogenic alkali granitoids are mainly distributed in the western segment of the Southwest Tianshan Mountains, and include the Huoshibulak alkali feldspar granite, with a zircon U–Pb age of 261.5 ± 2.7 Ma (Yang et al., 2001). Several NNE-trending diabase dykes, 440 to 1470 m long and 15 to 40 m thick, occur in the Sawayaerdun ore district. These have Triassic to Jurassic K–Ar ages of between 208 and 165 Ma (Liu et al., 2004).

The Neoproterozoic–Middle Ordovician period was a stage of “stable cover deposition”, when a phosphate siliceous sequence was deposited in the Early Cambrian, and littoral–neritic carbonate rocks and clastic rocks were formed in the Middle Cambrian–Middle Ordovician. The Late Ordovician to Late Silurian period was the stage of the “early paleo-South Tianshan ocean” (Gao et al., 1995), when the main part of the Southwest Tianshan belonged to the passive continental margin of the Tarim plate and received neritic clastic deposits and carbonate deposits, with a thick flysch and carbonate sequence developing in the Haerk area. At the end of the Silurian or at the beginning of the Early Devonian, the early paleo-Tianshan oceanic crust was subducted beneath the southern margin of the Ili microplate, resulting in development of paired metamorphic belts and island arc volcanic rocks in the Narat area. The Early Devonian to Early Carboniferous period was a stage of the formation of the “late paleo-Tianshan initial ocean basin”, when the extension of the passive continental margin of the Tarim plate resulted in the formation of the South Tianshan initial ocean basin and littoral–neritic clastic rocks and carbonate rocks were deposited, locally accompanied by volcanic eruptions. In the Early Carboniferous, the late paleo-Tianshan ocean closed (Gao et al., 1995), and continent–continent collision in the north of the South Tianshan Mountains gave rise to extensive collisional granites. In the Late Carboniferous, sedimentation styles were complicated, indicating the disappearance of the residual ocean basin and approaching of a continent plate (Liu et al., 1996). The continent–continent collision of the Tarim plate and Ili–Issyk Lake microplate took place in the Early Permian (Liu et al., 1996). During the collision, a number of ductile shear zones, thrust faults and thrust nappes developed in the Southwest Tianshan, accompanied by volcanism in the south of the Haerk area and Kalpin. Following the Early Permian, this region entered an intracontinental tectonic deformation stage. Magmatism was rather weakly developed, forming A-type granitoids. In the Triassic the region was peneplaned progressively. In the Jurassic–Cretaceous, the Tianshan orogen was in an extensional state (Shu et al., 2003).

3. Geology of the Bulong quartz–barite vein-type ore deposit

3.1. Stratigraphy

The strata exposed in the Bulong ore district belong to the Silurian and Upper Devonian Yimugantawu Formation and Kiziltag Formation, and the Upper Carboniferous Kangkelin Formation. The Silurian sequence is distributed in the southeastern part of the area and is composed of slightly metamorphic sandstone, siltstone and mudstone. The Upper Devonian Yimugantawu Formation is exposed in the central part of the ore district (Fig. 2), represented by a suite of purplish red and deep red, thin- to medium-bedded quartz siltstone and quartz fine sandstone and greyish green, thin-bedded siltstone. These rocks are intercalated with mudstone and shale and locally also intercalated with thin-bedded flysch conglomerate. The quartz–barite compound veins are dominantly hosted in the Upper Devonian Yimugantawu Formation. This is overlain by the Upper Devonian Kiziltag Formation which is a sequence of brick-red phyllitized quartz sandstone and siltstone intercalated with white quartz sandstone and locally intercalated with sandstone–conglomerate and shale; oblique bedding and ripple marks are well developed. A large barite

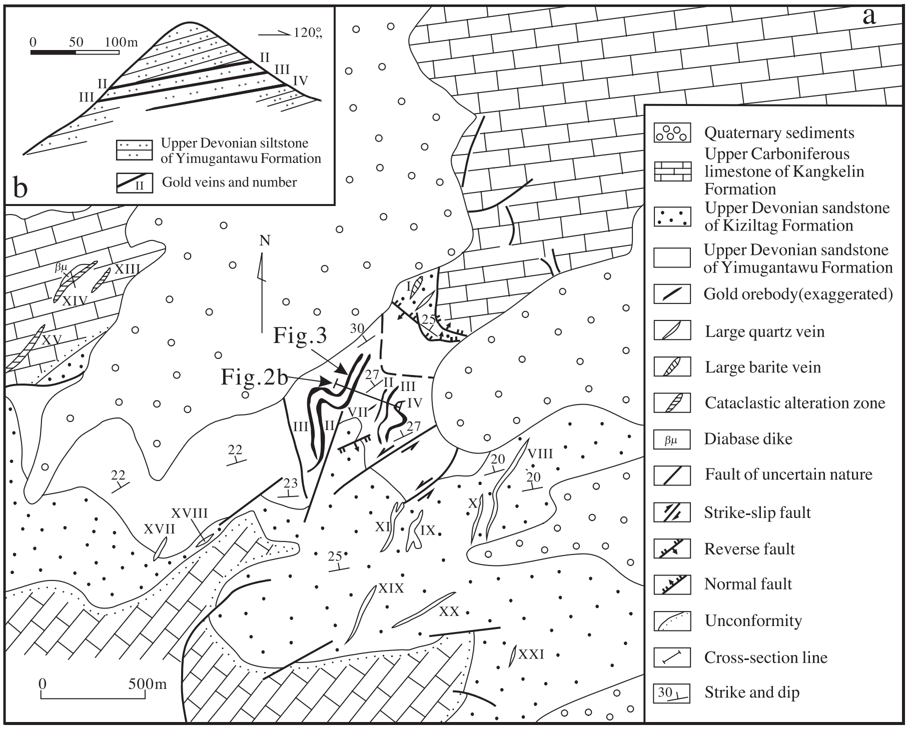

Fig. 2. (a) Simplified geologic map of the Bulong gold deposit (after No. 8 Geological Team, Xinjiang Bureau of Geology and Exploration, 1999) and (b) cross-section of gold veins. Gold mineralization is controlled by a series of gently tilted fractured zones. Four ore-bearing quartz–barite veins have been recognized in the Bulong ore district, they are defined as Nos. II, III, IV and VII, of which Nos. II, III and IV ore veins are larger in size.

vein and most large quartz veins (see below) are hosted in this formation. The Upper Carboniferous Kangkelin Formation is a sequence of grey, dark grey, massive to thick-bedded limestone and greyish black, thin- to medium-bedded limestone, locally intercalated with sandstone, siltstone and shale.

3.2. Tectonic characteristics and magmatic activity

The strata exposed in the Bulong ore district have been metamorphosed to low-grade conditions; this regional metamorphic event was caused by the early Permian collision. The age of regional metamorphism is 276 to 265 Ma according to ^{40}Ar/^{39}Ar dating of amphibole in plagioclase amphibolites from the Southwestern Tianshan Mountains (Liu et al., 1996).

The ore district is located in the northwestern limb of the Aerbaqieke box anticline (No. 8 Geological Party of the Xinjiang Bureau of Geology and Mineral Exploration and Development, 1995). The first-order Karateki fault is the main regional fault, which separates the Late Palaeozoic Southern Tianshan epicontinental basin from the Palaeozoic Kalpin foreland basin. The over 100 km long Karateki fault trends NE and dips NNW at 70 to 80°, and controls Late Hercynian magmatism, as well as Cretaceous, Paleogene and Neogene basin evolution. Several second-order faults, 100 to 700 m in length, are well developed in the Bulong ore district, relating to the first-order Karateki fault. The fault mainly trend NE–NNE, with NW–EW and SN-trending faults less abundant. Most ore veins are controlled by a series of these NE–NNE-trending, gently tilted fractured zones, but a 2.5 m thick large barite vein and 0.3 to 5.0 m thick large quartz veins in the ore district are controlled by a series of steeply dipping faults.

No magmatic rocks are exposed in the ore district, except for a rare NNE-trending diabase and diabase-porphyry dykes in the western part of the ore district and its surroundings. These Permian dykes are up to several hundred m long and tens of cm to several m in width. Two Variscan intermediate–acid sub-surface plutons occur about 6 km NE and SE of the area (Wang, 2001).

3.3. Ore veins

More than 20 veins and cataclastic alteration zones have been recognised in the Bulong ore district

(Fig. 2). Based on vein features and the relative timing of hydrothermal veins, these veins can be divided into four groups, ranging in age from oldest to youngest: large quartz veins (0.3–5.0 m thick), large barite veins (2.5 m thick), quartz–barite compound veins and carbonate veinlets. Gold orebodies are only hosted in quartz–barite compound veins (see below). Among these is the No. I vein, a large barite vein that occurs in a fracture zone in the Upper Devonian Kiziltag Formation in the northern part of the ore district. This vein trends NNE, is up to 2.5 m thick and intersects the strata at a high angle. The large barite vein is fractured, with rare pyrite in barite, and its average gold grade is 0.45 g/t. Nos. II, III and IV ore veins are gold-bearing quartz–barite compound veins; their basic features are shown in Table 1. These three veins are parallel to each other and occur ~20 to 50 m apart. They dip 320° to 10° at 10° to 28° and are largely concordant with the bedding of the strata. In plan view, they meander in a NE direction. Branching and converging may be observed locally for the No. III ore vein. Nos. II and III ore veins are exposed on both sides of a ridge (cross-section in Fig. 2b). The auriferous quartz–barite compound veins are almost pure barite veins, quartz veins, quartz–barite veins and some calcite–quartz–barite veins, but the pure barite veins pre-date the other veins on the basis of cross-cutting relationships. In vertical section (Fig. 3), pure barite veins can be observed in the centre, with quartz veins and barite–quartz veins situated in both the lower and upper portions of the compound veins. The gold orebodies mainly occur as quartz veins and quartz–barite veins. The orebodies appear as gently-tilted thin sheets, whose size is notably smaller than the compound veins in which they are hosted (Table 1). The average gold grade is 1.6 to 3.7 g/t, with a maximum of 22.4 g/t (No. 8 Geological Party of the Xinjiang Bureau of Geology and Mineral Exploration and Development, 1995).

The No. VII orebody has a cataclastic and brecciated texture and occurs in a barite-bearing quartz vein. It is the smallest orebody in the deposit and is characterized by the presence of abundant visible gold. Tens of gold grains can be observed in a typical hand specimen.

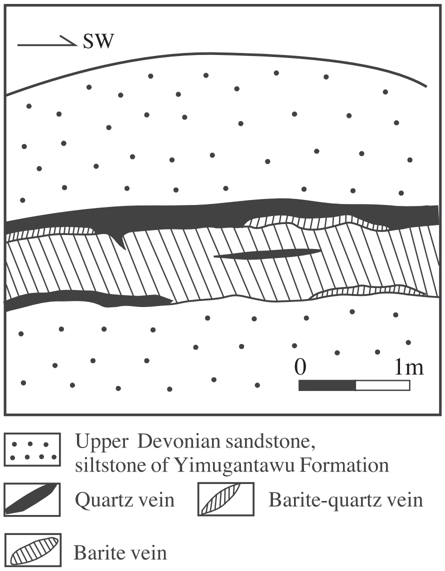

Fig. 3. Cross-section of the No. III ore vein. The pure barite vein is in the centre and quartz veins or barite–quartz veins in the lower and upper parts of the compound veins. The gold orebodies mainly occur as quartz veins and quartz–barite veins.

Nos. VIII–XI and XVII–XXI veins are large quartz veins, and occur in the Kizirtag Formation in the southern part of the ore district. The veins trend NNE to NE, striking obliquely to the strike of the strata; the veins dip steeply at angles of more than 60°. Minor pyritization is developed in the veins, and the gold grade is generally low (<0.5 g/t), although in rare cases grades may reach 1.0 to 5.8 g/t gold is very unevenly distributed. Gold mineralization of Nos. X and XI veins remains at sub-economic levels. No. VIII vein, nearly upright, is the largest among the quartz veins, being 450 m long and 0.8 to 5.0 m thick, and gold grades from 0.1 to 3.1 g/t. No. XI vein is 250 m in length and 0.3 to 1.2 m thick, with gold grades of about 0.1 to 0.5 g/t with a maximum of 1 g/t.

Table 1
Features of ore veins and gold orebodies in the Bulong gold deposit in Akqi county

Ore vein number	Quartz–barite vein			Gold orebody			
	Length/m	Thickness/m	Dip/angle	Length/m	Width/m	Thickness/m	Average Au grade(g/t)
II	230–660	0.50–1.0	320°–10°/10°–28°	85–450	240	0.34	3.72
III	400–630	0.8	320°–10°/10°–25°	280–400	360	0.5	2.74
IV	310	1	320°–0°/10°–25°	81		0.42	1.64
VII	15	0.5	42°/20°	15		0.5	5.66

After No. 8 Geological Party, Xinjiang Bureau of Geology and Mineral Exploration and Development (1999).

3.4. Mineralization periods and stages

Based on cross-cutting relationships of the ore veins, mineral assemblages, paragenetic sequence and ore fabrics, the ore-forming process can be divided into two mineralization periods: hydrothermal and supergene. The hydrothermal period can be further divided into four mineralization stages:

Stage I is the quartz stage, characterized by the occurrence of large quartz veins, 0.3 to 5.0 m thick, (Fig. 4A) along steeply dipping faults. The mineral assemblage is simple, dominated by quartz with minor spotted pyrite and ankerite. Gold mineralization is low and the gold grade in these veins is commonly <0.5 g/t.

Stage II is represented by the barite stage and is characterized by the presence of pure barite veins, distributed in the centre of quartz–barite compound veins or forming single large barite veins (e.g., No. I vein; Fig. 4B). The principal mineral is barite, with minor pyrite and siderite. The barite formed during this stage is white and coarse in grain size, and commonly occurs as euhedral crystals. Gold grades are 0.3 to 3 g/t.

Stage III is the barite–quartz stage, which can be further divided into two mineralization substages; a siderite–quartz substage and a quartz–barite–calcite substage. The siderite–quartz substage is characterized by the formation of auriferous quartz veins (Fig. 4C). The quartz–barite–calcite substage is characterized by the presence of barite–quartz veins and calcite–barite–quartz veins. Calcite–barite–quartz veins mostly occur as lenses or patches. The veins range in thickness from several up to 50 cm. These veins are distributed in the upper, lower and marginal parts of the ore veins or form single ore veins (e.g., No. VII). In the contact zone between the barite veins and quartz veins or barite–quartz veins, veinlets of the latter can be seen to penetrate the former in outcrop (Fig. 3), and pure barite veins are crosscut by the quartz veinlets or stockworks of the microscope scale. The mineral assemblage includes calcite, siderite, ankerite, pyrite and native gold. Barite is mostly anhedral, granular, 0.2 to 0.4 mm in size, and in mosaic contact with quartz. This stage was the main stage of gold mineralization in the Bulong deposit. Gold grades typically range from 1.0 to 22.3 g/t. The ore types of stage III are simple, and comprise mainly auriferous quartz–barite vein and auriferous quartz vein types and a rare auriferous breccia type (e.g., No. VII ore vein). Ores mainly have euhedral, subhedral to anhedral granular, metasomatic to

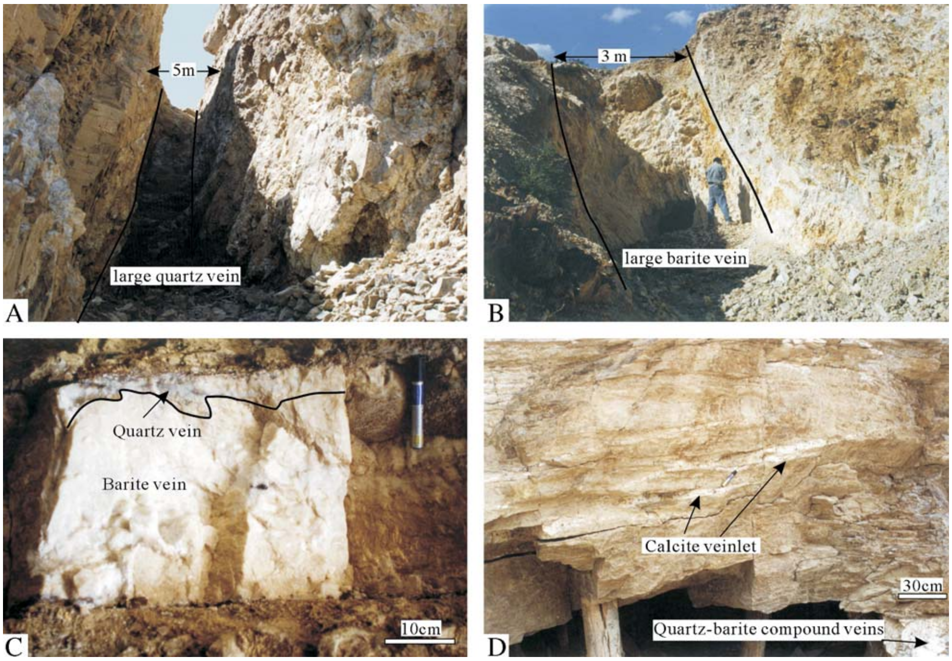

Fig. 4. Photographs of different types of veins from the Bulong gold deposit showing: (A) No. IX vein is a large quartz vein, which is steeply dipping and oblique to the strike of the strata; (B) No. I vein is a large barite vein, occurring in a fracture zone in the Upper Devonian Kiziltag Formation; (C) No. III vein is a quartz–barite compound veins (gold ore vein), quartz vein is distributed in the upper part. In the contact zone between the quartz vein and barite vein, the quartz veinlets can be seen to penetrate into the barite vein; (D) Calcite veinlets spread mainly along the fractures in the wall rocks.

skeletal texture, and disseminated, veinlet-stockwork, vein, massive and brecciated structures. The brecciated structure only occurs in No. VII orebody, with siltstone and barite clasts and quartz cement. Macroscopic visible gold grains are distributed either at the contacts between quartz and clasts, or in honeycomb pores that have resulted from weathering of sulphides. Ore minerals account for <1 vol.% of the ore-bearing veins, and include pyrite and native gold, with minor chalcopyrite, bornite and malachite. Gangue minerals are mainly barite and quartz; siderite, limonite, calcite and ankerite are less abundant and sericite, chlorite, and feldspar occur locally.

Stage IV is the late-stage ankerite–calcite veinlet stage (carbonate stage), in which mainly calcite veinlets or ankerite veinlets formed (Fig. 4D). These veinlets are several to 50 mm wide and are mainly spread along fractures in the wall rocks, rarely penetrating into ore veins. This stage represents the final stage of the ore-forming process; the gold content in these veinlets remains low (0.1 to 0.2 g/t).

3.5. Wall rock alteration

Wall rock alteration in the Bulong deposit includes silicification, pyritization, sideritization, sericitization, chloritization, calcitization and ankeritization. Of these, silicification, pyritization, and sideritization are closely associated with gold mineralization. Silicification is well developed in the deposit and can be divided into at least two phases. During the first phase siltstone recrystallized into quartz aggregates, forming a layer, 1 to 2 mm thick, in wall rocks adjacent to the ore veins. The second phase silicification is manifested by irregular quartz veinlets and calcite–quartz veinlets between 1 and 5 mm thick. Pyritization mainly occurs in wall rocks close to ore veins, and there is a positive correlation between pyrite content and proximity to ore veins. Small amounts of disseminated pyrite occur in the auriferous (barite) quartz veins, and rare pyrite can be observed in the large quartz veins. Pyrite in the ore veins is fine-grained (≤0.5 mm in diameter), but coarser in the wall rocks, generally 0.5 to 1.0 mm in size — rarely up to 8 mm. Sericitization is best developed in the wall rocks close to ore veins, and shows a fine flaky texture.

3.6. Modes of occurrence of gold

Gold occurs in the form of native gold and has three modes of occurrence: (1) intergranular gold between quartz grains or between quartz and barite grains, (2) fissure gold distributed in fissures within pyrite, and (3) gold hosted in quartz grains or barite grains.

Native gold is gold-yellow in colour, with a strong metallic lustre, and mainly occurs as grains, irregular dendritic aggregates and sheets and rare incomplete cubic crystals. The grain size of primary gold is generally <0.01 mm. Microprobe analysis of a typical native gold grain gives the following composition (wt.%): Au 97.85, Ag 0.60, Cu 0.13, Zn 0.13, Cd 0.09, Sb 0.18, Fe 0.05, Co 0.08, Te 0.05, Mo 0.02, S 0.02 and Ni 0.22 (No. 8 Geological Party of the Xinjiang Bureau of Geology and Mineral Exploration and Development, 1995). The fineness of gold is <0.994.

4. Fluid inclusion studies

4.1. Methods

The petrographic characteristics of fluid inclusions were studied and types and assemblages of fluid inclusions were distinguished by optical microscopy of doubly polished sections (~200 to 300 μm in thickness). Microthermometric measurements were carried out on a Linkam THMSG 600 programmable heating–freezing stage (−196 to +600 °C) at the Key Laboratory of Research Center for Mineral Resources, Institute of Geology and Geophysics, Chinese Academy of Sciences. The stage was calibrated using synthetic fluid inclusions. The heating rate was 0.1 to 1 °C/min below 10 °C, whereas rates were about 3 to 5 °C/min between 10 to 31 °C, with a reproducibility of ±0.1 °C. The heating rate was 5 to 10 °C/min at higher temperatures (>100 °C), with a reproducibility of ±2 °C.

4.2. Inclusion types and characteristics

Fluid inclusions were examined in 30 samples from all four mineralization stages in the Bulong deposit. Fluid inclusions were abundant in quartz and barite grains of stages I to III, and less abundant in calcite grains of stage IV veins. Quartz, barite and calcite grains were not found to have undergone deformation or recrystallization. The observed fluid inclusions can be classified into types of H_2O–NaCl and H_2O–CO_2 ($\pm CH_4/N_2$)–NaCl types based on their phase relationships and chemical compositions at room temperature. The H_2O–NaCl type can be further divided into two-phase (L+V) and polyphase inclusions with daughter crystals. The H_2O–CO_2 ($\pm CH_4/N_2$)–NaCl type can be divided into three-phase CO_2-type, CO_2-rich type and multiphase inclusions (high salinity, aqueous, carbonic inclusions). So, in all, five types of fluid inclusions can be distinguished and have been assigned herein as types I, II, III, IV and V, respectively. Inclusion types and characteristics are listed in Table 2 and shown in Fig. 5.

Fluid inclusions in the quartz stage (stage I) are dominantly three-phase CO_2-type inclusions (type III), with rare H_2O–CO_2-daughter crystal-bearing polyphase inclusions (type V). These inclusions are primary or pseudosecondary, and are interpreted to contain the fluid that deposited the early quartz of stage I. There are minor amounts of two-phase ($L+V$) inclusions and polyphase inclusions with daughter crystals (type II) in quartz of stage I. These fluid inclusions show characteristics that suggest a secondary origin. At room temperature, most type III inclusions (Fig. 5C–E) consist of three phases (liquid water + liquid CO_2 + CO_2-rich vapor), and some of the two-phase fluid inclusions also nucleated a third phase during slight cooling below room temperature. Type V inclusions (Fig. 5H) consist of four phases (liquid water + liquid CO_2 + CO_2-rich vapor + daughter crystal) at room temperature. The CO_2 volumetric proportion ranges from 5% to 20%, with a vapor/liquid CO_2 ratio of 5% to 60%. Microscopic study suggests that the daughter crystals are commonly halite. These inclusions are relatively rare and occur only in quartz grains formed during the quartz stage.

Primary or pseudosecondary fluid inclusions in the barite stage mostly contain two-phase aqueous-type inclusions, and coexists with minor daughter mineral-bearing inclusions. These inclusions are interpreted to contain the fluid that deposited barite of stage II.

Fluid inclusions representative of the main mineralization stage (stage III) mostly contain two-phase aqueous-type inclusions, with minor daughter mineral bearing inclusions (Fig. 5F, G), three-phase CO_2-type inclusions (type III) and CO_2-rich type inclusions (type IV, carbonic liquid and vapor constitute 90% to 95% of the total volume of each inclusion). Vapor-rich aqueous-type inclusions occur locally in quartz of stage III, with a degree of fill of <0.30, that homogenizes into the vapor phase when heated. This type of inclusion coexists with two-phase aqueous inclusions, but it is rare. Type I inclusions (Fig. 5A, B) are most abundant in the main mineralization stages and usually coexist with minor daughter mineral-bearing inclusions. Although fluid inclusions are commonly present as isolated groups within the transparent mineral grains, they can also occur in the primary growth zones of quartz crystals, and therefore are considered to be primary in

Table 2
Inclusion types and characteristics of the Bulong gold deposit

Type	Name	Component	Size (μm)	Shape	Degree of fill	Characteristics of daughter mineral	Distribution
I	Two-phase type ($L+V$)	Aqueous liquid and vapor bubbles	2–12, rarely 15–30	Negative crystal, incomplete negative crystal shaped elliptical and irregular shapes	0.7–0.95, mainly 0.85–0.95		Quartz, barite and calcite grains from stages II, III and IV
II	Daughter mineral-bearing polyphase inclusions	Vapor, liquid and daughter crystals (halite)	7–20	Irregular	0.85–0.95	Halite occurs in cubic, rectangular and equant shapes; from <1 to about 4 μm	Quartz and barite grains formed in stages I, II and III
III	Three-phase CO_2-type	Aqueous liquid, carbonic liquid and vapor	5–20, rarely up to 32	Elliptical, irregular, negative crystal shapes, incomplete negative crystal shaped	0.7–0.95		Quartz and barite grains formed in stages I and III
IV	CO_2-rich type inclusions	Liquid CO_2 and vapor CO_2	4–10	Irregular	0.05–0.10 (H_2O)		Quartz grains formed in stages III
V	High salinity aqueous carbonic inclusions	Liquid water, liquid CO_2, CO_2-rich vapor and daughter crystal	6–40, mainly <20	Elliptical, irregular, incomplete negative crystal shaped	0.80–0.95 (H_2O)	Halite has cubic and rectangular shapes; 3–6 μm	Quartz grains formed in the quartz stage

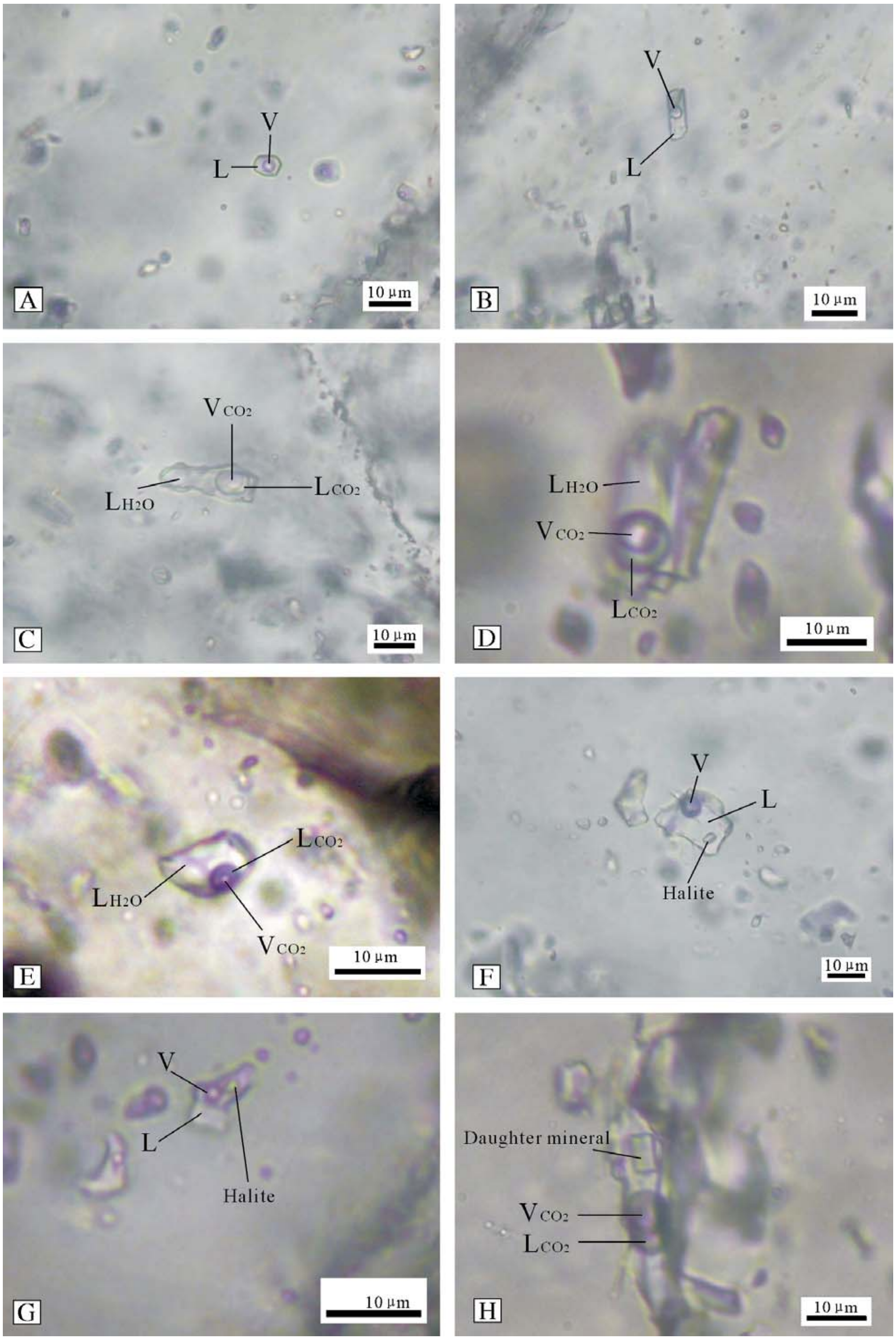

Fig. 5. Photomicrographs of fluid inclusions in quartz and calcite from the Bulong gold deposit: (A) Two-phase vapor–liquid inclusions that homogenizes to a liquid phase; (B) Two-phase vapor–liquid inclusions in calcite; (C), (D) and (E). Three-phase CO_2-type inclusions and homogenization to a liquid; (F) and (G). Daughter mineral-bearing inclusions. H. Multiphase daughter mineral (halite)–L_{CO2}–V_{CO2}–L_{H2O} inclusion.

origin. In a few cases, fluid inclusions occur along microcracks within transparent mineral grains, but these are not found cutting crystal boundaries. Although direct physical contact of fluid inclusions with gold grains was not observed, gold grains are intergrown with pyrite or quartz–barite grains in stage III assemblages; thus, these H_2O–NaCl type inclusions are considered to represent the gold-bearing fluids.

There are only two-phase aqueous-type inclusions in the late-stage calcite veinlet. These inclusions are interpreted to contain a fluid trapped late in the hydrothermal history of the system.

4.3. Microthermometric results

4.3.1. NaCl–H_2O fluid inclusions

A total of 274 NaCl–H_2O inclusions in 20 samples from three mineralization stages were measured, and the data are summarized in Table 3 and Figs. 6–8. All two-phase aqueous inclusions homogenize into the liquid phase.

Homogenization temperatures for the barite stage range between 161 and 260 °C with the majority of Th ranging between 180 and 240 °C. The ice-melting temperatures are in a range of −5.6 to −11.2 °C. The salinities determined from melting temperatures of the fluid inclusions range from 8.68 to 15.17 wt.% NaCl equiv (Bodnar, 1992). Using final homogenization temperatures and the above salinities, the resulting densities of the aqueous phase range between 0.90 and 1.00 g/cm^3, using the NaCl–H_2O reference table of Liu and Shen (1999).

The homogenization temperatures of 126 aqueous inclusions in quartz of the siderite–quartz substage (stage IIIa) range from 187 to 381 °C and cluster between 220 to 320 °C, with a peak temperature of 280 °C. The salinities of the aqueous inclusions determined from 67 ice-melting temperatures of −4.6 to −14.0 °C range from 7.31 to 17.79 wt.% NaCl equiv at a peak around 14 wt.% NaCl equiv, and fluids densities between 0.73 and 0.98 g/cm^3.

Microthermometric measurements of fluid inclusions in quartz, barite and calcite formed in the quartz–barite–calcite substage (stage IIIb) yielded homogenization temperatures ranging from 159 to 390 °C and clustering between 180 and 320 °C, with a peak around 240 °C, salinities of 5.26 to 19.29 wt.% NaCl equiv and fluid densities between 0.77 and 1.03 g/cm^3.

The homogenization temperature of two-phase inclusions in the carbonate stage range from 183 to 320 °C and show a bimodal distribution of two temperature intervals, i.e., from 190 to 220 °C and from 260 to 320 °C. The salinity estimated from ice-melting data of two-phase inclusions range from 6.01 to 9.86 wt.% NaCl equiv and fluid densities between 0.75 and 0.96 g/cm^3.

The polyphase inclusions are small in size, with correspondingly very small daughter crystals. Therefore, phase changes were measured in only five inclusions in quartz and barite. The polyphase inclusions are

Table 3

Microthermometric data for the different types of the fluid inclusions from the Bulong gold deposit

Phase		Mineral	Type	T_{mCO2} (°C)	T_{mcl} (°C)	T_{hCO2} (°C)	T_{htot} (°C)		T_{mice} (°C)	T_{mh} (°C)	Salinity (wt.% $NaCl_{eq}$)		Degree of fill	Density (g/cm^3)
							Range	Mean			Range	Mean		
Quartz stage (Stage I)		Quartz	III	−58.1 to −58.9	6.3–8.8	16.1–27.1					2.44–6.96	4.75	0.70–0.95	0.67–0.80*
		Quartz	V	−58.3 to −58.9		19.6–27.9				132–195	29.02–31.66	30.10	0.80–0.90	0.66–0.77*
Barite stage (Stage II)		Barite	I				161–260	219	−11.2 to −5.6		8.68–15.17	11.92	0.70–0.95	0.90–1.00
		Barite	II				161–221	189		209–330	32.36–40.20	36.36	0.90–0.95	1.069–1.112
Barite–quartz stage (Stage III)	Siderite–quartz substage III_a	Quartz	I				187–381	271	−14.0 to −4.6		7.31–17.79	12.81	0.75–0.95	0.73–0.98
		Quartz	II				307			396	46.2		0.90	1.08
		Quartz	III	−58.2 to −58.4	7.0	19.6–21.0	272–298				5.76		0.30–0.90	0.77
		Quartz	IV	−58.4		2.9–3.6							<0.05	0.90–0.89*
	Quartz–barite–calcite substage III_b	Quartz	I				179–390	261	−15.8 to −5.2		8.14–19.29	14.90	0.75–0.95	0.77–0.98
		Barite	I				159–249	197	−13.5 to −8.1		11.81–17.34	15.00	0.90–0.95	0.97–1.03
		Barite	II				175			198	31.80		0.90	1.12
		Calcite	I				181–307	257	−7.4 to −3.2		5.26–10.98	8.30	0.70–0.95	0.79–0.95
Carbonate stage (Stage IV)		Calcite	I				183–321	233	−6.5 to −3.7		6.01–9.86	7.36	0.90–0.95	0.75–0.96

T_{mCO2} — melting temperature of CO_2; T_{mcl} — melting temperature of CO_2 clathrate; T_{hCO2} — partial homogenization temperature of CO_2 into liquid; T_{htot} — total homogenization temperature; T_{mice} — melting temperature of ice; T_{mh} — temperature of halite melting; *— CO_2 density; H_2O–NaCl fluid inclusions include type I and II inclusions; H_2O–CO_2 (±CH_4/N_2)—NaCl fluid inclusions include type III, IV and V inclusions.

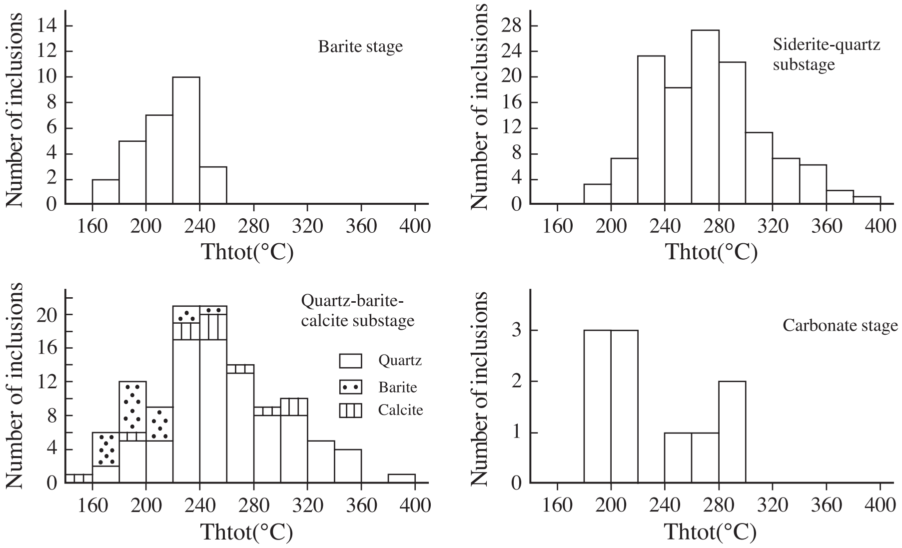

Fig. 6. Histograms of homogenization temperature for the fluid inclusions in the Bulong gold deposit.

supersaturated saline inclusions, in which the melting temperature of daughter crystals are higher than the vapor–liquid homogenization temperatures. According to the appropriate parameter table of Liu and Shen (1999), the salinities range from 32.36 to 46.20 wt.% NaCl equiv, which indicate that the fluids are hyperhaline (Hedenquist and Lowenstern, 1994). The daughter mineral-bearing polyphase inclusions with estimated salinities show relatively high densities of 1.07 to 1.11 g/cm^3.

4.3.2. H_2O–CO_2 (± CH_4/N_2)–NaCl fluid inclusions

A total of 32 CO_2–H_2O ± CH_4 inclusions were measured in quartz and barite. Of these, 24 inclusions were from stage I and eight from stage III. All of these inclusions homogenized to the aqueous liquid-phase. The melting temperatures of solid CO_2 typically range from −58.1 to −58.9 °C, suggesting a CO_2-rich composition with minor amounts of CH_4 or N_2 (Burruss, 1981). The CO_2 partial homogenization temperatures of CO_2 type inclusions range between 2.9 to 27.1 °C into liquid with a peak distribution at 21 °C (Fig. 9). The clathrate-melting temperatures obtained from inclusions range from 6.3 to 8.8 °C at a peak of 7.8 °C (Fig. 10). The salinities of the three-phase inclusions, were calculated using the equation of Darling (1991), assuming no significant effects from minor CH_4 or N_2. The salinities of fluids from the quartz stage range between 2.44 to 6.96 wt.% NaCl equiv (Fig. 7). Almost all the analysed inclusions of this phase decrepitated prior to homogenization, and we could not calculate total densities for the three-phase fluids of stage I and III.

Six high salinity aqueous carbonic inclusions (type V) in quartz from stage I were measured, and the data

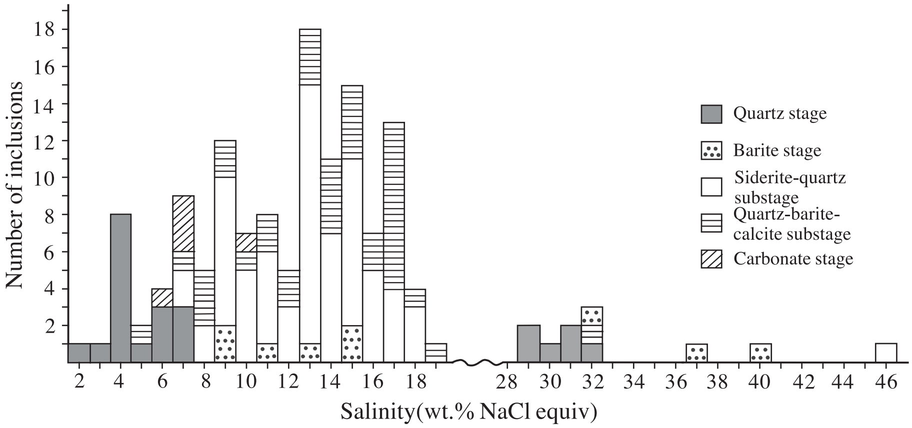

Fig. 7. Histograms of all salinity for the fluid inclusions in the Bulong gold deposit.

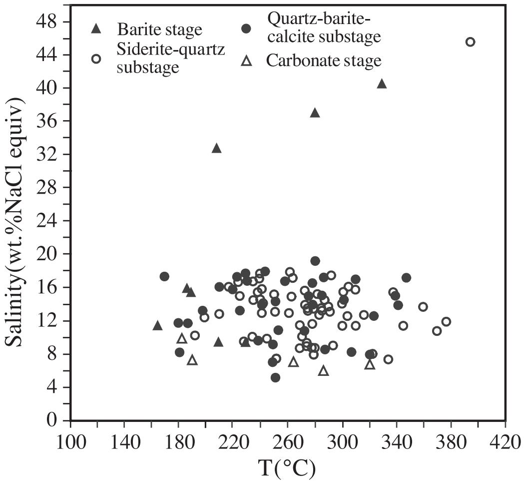

Fig. 8. Diagram of homogenization temperatures versus salinity of fluid inclusions in the Bulong gold deposit.

are summarized in Table 3 and Figs. 7–9. The melting temperatures of CO_2 range from −58.3 to −58.9 °C; partial homogenization of CO_2 liquid+CO_2 vapor to liquid occurs between 19.6 and 27.9 °C (Fig. 9). The daughter crystals melted at 132 to 195 °C. Upon heating, all of these inclusions decrepitated at temperatures from 210 to 251 °C prior to final homogenization. Thus, total densities and detailed compositions (X_{CO2}) of high salinity aqueous carbonic inclusions could not be calculated. According to the melting temperatures of daughter crystals (halite), we estimate the salinities to range from about 29 to 32 wt.% NaCl equiv.

The composition of fluid inclusions was analyzed in 12 quartz samples from the main mineralization stages in the Bulong gold deposit at the Key Laboratory of Research Center for Mineral Resources, Institute of Geology and Geophysics, Chinese Academy of Sciences. The gas in fluid inclusions was analyzed by the quadrupole mass spectrometer method (Zhu et al., 2003), and the liquid composition of fluid inclusions are analyzed by ion chromatographic analysis. The gas components of fluid inclusions are mainly H_2O (94.5 to 98.7 mol%) and CO_2 (1.3 to 4.9 mol%), with minor amounts of N_2, CH_4, C_2H_6, H_2S, etc. The liquid components of fluid inclusions are mainly Na^+ and Cl^-, and Ca^{2+}, K^+, Mg^{2+}, and SO_4^{2-} are less abundant, $Na^+/K^+>1$, $Cl^->F^-$ and $SO_4^{2-}/(F^-+Cl^-)<1$, belonging to the H_2O–NaCl–CO_2 system.

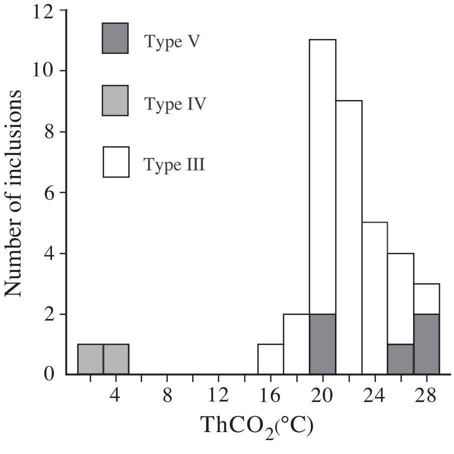

Fig. 9. Histogram of CO_2 homogenization temperatures in the Bulong gold deposit.

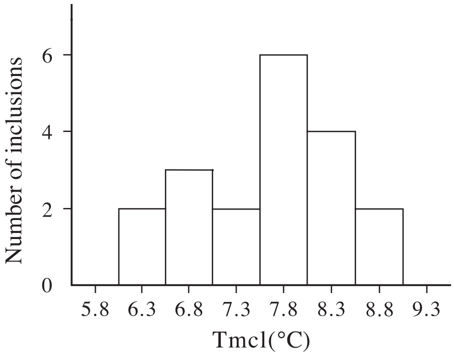

Fig. 10. Histogram of melting temperatures of CO_2 clathrates in the type III inclusions.

5. Stable isotope analysis

5.1. Samples and analytical methods

All mineral separates were examined under the binocular microscope prior to isotopic analysis to ensure their purities were >99%. Ten fresh pyrite samples (five from the quartz stage, five from pyritized wall rocks near orebodies) and ten barite samples (from the barite stage) were collected for sulfur isotope measurements. Cu_2O was used as the oxidizer for the preparation of sulphide samples (Robinson and Kusakabe, 1975). Sulphate minerals were purified to pure $BaSO_4$ by the carbonate–zinc oxide semi-melt method, and then SO_2 was prepared by the V_2O_5 oxide and Cu_2O method. The SO_2 released was measured for sulfur isotopes.

Ten samples were selected for He and Ar isotope measurements of which five were collected from the pyritized wall rocks near orebodies and five from the quartz stage of the large quartz vein. Helium and Ar isotopes were analyzed at the Stable Isotope Laboratory, Institute of Mineral Resources, Chinese Academy of Geological Sciences. The analytical procedure is described by Li et al. (2002) and Mao et al. (2002a). The helium isotopic composition was measured on a MI-1201 IG inert gas mass spectrometer. ^4He was received by a Faraday cup and ^{3}He by an electron multiplier. The amplification coefficient of the electronic multiplier was 1×10^5 and its resolution was 1200, so that the peaks of ^{3}He and HD+H_3 can be completely separated from each other, without the need to correct for HD+H_3. Ar was desorbed on the charcoal finger and separated from Xe at −78 °C. ^{40}Ar was received by a Faraday cup and ^{36}Ar and ^{38}Ar by an electronic multiplier. The standard gas was measured before analyzing the samples, and the measurement results of samples were normalized to the standard gas, purified air and periodically examined during measurements. All analytical results are based on the international atmosphere standard, whose ^{3}He/^{4}He ratio is 1.40×10^{-6}. All the results of helium were given as ^{3}He/^{4}He and R/R_a ratio, where R is the ^{3}He/^{4}He ratio of the sample and R_a is that of the air. The blank level of ^{4}He was 2×10^{-11} cm^3 STP, the blanking ^{3}He/^{4}He ratio was 1×10^{-6} and the blank level of ^{40}Ar was 5×10^{-9} cm^3 STP. The effect of the blank on the measurement result was negligible. The analytical precision of the standard gas was 1%.

Fourteen samples were selected for carbonate, hydrogen and oxygen isotope measurements, of which eight were collected from the siderite–quartz substage of the auriferous quartz veins and six from the quartz–barite–calcite substage of the auriferous barite–quartz veins and calcite–quartz vein from Nos. II, III, IV, and VII ore veins. For oxygen isotope analyses of silica and silicates, CO_2 was prepared by the BrF_5 method described by Clayton and Mayeda (1963). For analysis of hydrogen isotopes, the water in fluid inclusions was released by the thermal decrepitation method. The water was then reacted with Zn at 400 °C to produce H_2 (Coleman et al., 1982), which was collected in sample tubes with activated charcoal at liquid N_2 temperatures (Mao et al., 2002b). For analysis of carbonate isotopes, the CO_2 in fluid inclusions was also released by decrepitation. The $\delta^{13}C_{PDB}$ values of samples were directly obtained from the CO_2 (CH_4 was separated). All SO_2, CO_2, and H_2 were analyzed in a Finningan MAT 251 mass spectrometer, at the Stable Isotope Laboratory of the Institute of Mineral Resources, Chinese Academy of Geological Sciences. Analytical reproducibility in this study is ±0.2‰ for S, O and C isotopes, and ±2‰ for H isotopes.

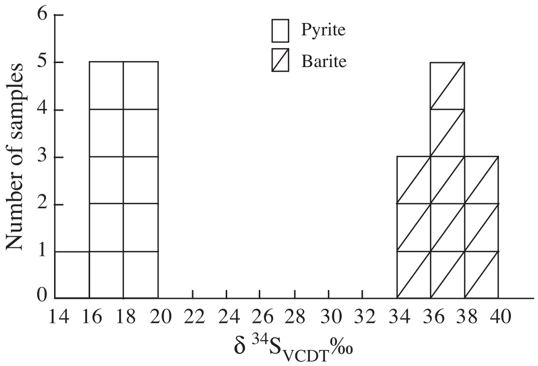

Fig. 11. Histogram of sulfur isotopic compositions of the Bulong gold deposit.

5.2. Results

5.2.1. Sulfur isotopic composition

The δ^{34}S values of pyrite range from 14.6‰ to 19.2‰ with a mean of 17.6‰. Pyrite from wall rocks near the gold vein range from 14.6‰ to 17.7‰ with a mean of 16.5‰, and those of pyrite from the large quartz vein are slightly higher, ranging from 18.5‰ to 19.2‰ with a mean of 18.9‰. The δ^{34}S values of barite range from 35.0‰ to 39.6‰ with a mean of 37.3‰ (Table 4; Fig. 11).

Table 4
Compositions of the sulfur isotope in the Bulong gold deposit

Ser. no.	Sample	Mineral	$\delta^{34}S_{CDT}$ (‰)	Ser. no.	Sample	Mineral	$\delta^{34}S_{CDT}$ (‰)
1	BL-3-13	Pyrite	16.6	12	BL-2-2	Barite	37.5
2	BL-3-14	Pyrite	16.8	13	BL-2-6	Barite	37.8
3	BL-3-15	Pyrite	14.6	14	BL-3-4	Barite	38.8
4	BL-3-16	Pyrite	16.0	15	BL-3-6	Barite	35.8
5	BL-3-18	Pyrite	17.1	16	BL-3-7	Barite	35.0
6	BL-8-1	Pyrite	19.1	17	BL-3-19	Barite	39.6
7	BL-8-2	Pyrite	19.2	18	BL-3-24	Barite	35.4
8	BL-8-3	Pyrite	19.2	19	BL-3-43	Barite	39.1
9	BL-8-4	Pyrite	18.7	20	BL-4-5	Barite	36.8
10	BL-8-5	Pyrite	18.5	21	BL-4-6-1	Barite	37.2
11	BL-41-1	Pyrite	17.7	22	BL-12	Barite	36.8

Note: Serial no. 11 and 22 are after Zheng et al., 1996; 1–5 from the pyritized wall rock near the gold lode; 6–10 from the auriferous large quartz vein.

Table 5
Helium and argon isotopic compositions of fluid inclusions in pyrite from the Bulong gold deposit

Ser. no.	Sample no.	Mineral	$(^3He/^4He)\times10^{-7}$	$^4He\times10^{-6}$ cm^3 STP/g	R/R_a	$^{40}Ar/^{36}Ar$	$^{40}Ar/^{38}Ar$	$^{36}Ar/^{38}Ar$	$^{40}Ar\times10^{-7}$ cm^3 STP/g	$^{40}Ar/^4He$	He_{mantle} (%)
1	BL-3-13	Pyrite	3.32 ± 0.53	8.02	0.24	376 ± 4	2068 ± 10	5.52 ± 0.04	6.85	0.085	2.8
2	BL-3-14	Pyrite	8.38 ± 1.26	2.16	0.60	351 ± 3	1913 ± 24	5.28 ± 0.06	2.54	0.118	7.5
3	BL-3-15	Pyrite	5.41 ± 0.96	10.78	0.39	338 ± 3	1878 ± 13	5.56 ± 0.05	4.13	0.038	4.7
4	BL-3-16	Pyrite	9.28 ± 1.91	1.24	0.66	356 ± 6	1978 ± 47	5.53 ± 0.23	5.11	0.412	8.3
5	BL-3-18	Pyrite	7.79 ± 1.78	0.99	0.56	369 ± 6	2025 ± 25	5.37 ± 0.20	0.15	0.015	6.9
6	BL-8-1	Pyrite	11.47 ± 2.14	4.56	0.82	429 ± 3	2296 ± 25	5.32 ± 0.16	8.20	0.18	10.3
7	BL-8-2	Pyrite	11.04 ± 1.00	2.68	0.79	395 ± 6	2186 ± 28	5.53 ± 0.03	3.14	0.117	9.9
8	BL-8-3	Pyrite	10.24 ± 2.82	3.58	0.73	427 ± 34	2349 ± 112	5.56 ± 0.41	5.27	0.147	9.2
9	BL-8-4	Pyrite	7.70 ± 1.10	3.94	0.55	463 ± 9	2504 ± 40	5.38 ± 0.02	8.76	0.222	6.8
10	BL-8-5	Pyrite	8.90 ± 0.67	3.25	0.64	471 ± 9	2533 ± 17	5.34 ± 0.10	6.21	0.191	7.9

5.2.2. Helium and argon isotopes

The He and Ar isotopic compositions of fluid inclusions in pyrite from the Bulong gold deposit are shown in Table 5. The normalized $^3He/^4He$ ratios of fluid inclusions in pyrite are 0.24 to 0.82 (R/R_a), $^{40}Ar/^{36}Ar$ ratios are 338 to 471 and $^{40}Ar/^4He$ ratios are 0.02 to 0.22 with a mean of 0.153, except for one sample which gives 0.41. The data show that the isotope compositions of pyrite in the wall rocks near orebodies are somewhat different from those of the large quartz veins. For the former, the R/R_a ratios of fluid inclusions are 0.24 to 0.66 with a mean of 0.49, $^{40}Ar/^{36}Ar$ ratios are 338 to 376, and $^{40}Ar/^4He$ ratios are 0.02 to 0.12, except for sample BL-3-16 whose $^{40}Ar/^4He$ ratio is 0.41. For the latter, those ratios are slightly higher: the R/R_a ratios are 0.55 to 0.82 with a mean of 0.71, $^{40}Ar/^{36}Ar$ ratios are 395 to 471 and $^{40}Ar/^4He$ ratios are 0.12 to 0.22. The data are consistent with the marked differences in the geological characteristics, gold content and ore-forming stages of both quartz–barite compound veins and large quartz veins.

5.2.3. Carbon, oxygen and hydrogen stable isotopes

The analytical results of C, O and H stable isotope analyses of the Bulong gold deposit are shown in Table 6. The $\delta^{13}C_{PDB}$ values of fluid inclusions in quartz vary between −4.6‰ and −1.4‰ with an average of −3.6‰. The $\delta^{13}C_{PDB}$ values range from −4.5‰ to −3.3‰ with a mean of −3.7‰ for the siderite–quartz substage and −4.6‰ to −1.4‰ with a mean of −3.3‰ for the quartz–barite–calcite substage. The $\delta^{18}O_{SMOW}$ values of quartz range from 17.2‰ to 21.1‰ with a mean of 19.4‰ for the siderite–quartz substage and from 17.2‰ to 20.4‰ with a mean of 18.6‰ for the quartz–barite–calcite substage, respectively.

Using the quartz–water fractionation equation $1000\ln\alpha=3.38\times10^6T^{-2}-3.40$ (Clayton et al., 1972) and the average homogenization temperature of fluids inclu-

Table 6
Carbon, oxygen and hydrogen isotopic data of the Bulong gold deposit

Ore vein no.	Sample no.	Vein	Mineral	δD (‰ SMOW)	$\delta^{18}O_{qtz}$ (‰ SMOW)	T_h (°C)	$\delta^{18}O_{fluid}$ (‰)	$\delta^{13}C_{CO2}$ (‰ PDB)
II	BL-2-1	Quartz vein	Quartz	−70	18.5	271	10.5	−3.5
II	BL-2-3	Quartz–barite vein	Quartz	−64	17.6	258	9	−1.4
II	BL-2-4	Quartz vein	Quartz	−64	20.4	271	12.4	−3.8
II	BL-2-7	Quartz vein	Quartz	−61	17.2	258	8.6	−3.5
II	BL-2-12	Quartz–barite vein	Quartz	−63	19.9	262	11.5	−2.9
III	BL-3-1	Calcite–quartz vein	Quartz	−70	17.9	298	10.9	−3.6
III	BL-3-2	Quartz vein	Quartz	−63	18.6	312	12.1	−3.8
III	BL-3-3	Quartz–barite vein	Quartz	−63	18.7	242	9.4	−3.6
III	BL-3-29	Quartz–barite vein	Quartz	−66	17.2	220	6.7	−4.6
III	BL-3-36	Quartz vein	Quartz	−58	19.6	281	12	−3.6
IV	BL-4-2	Quartz vein	Quartz	−63	20.6	254	11.8	−4.0
IV	BL-4-10	Quartz vein	Quartz	−60	21.1	313	14.7	−4.5
IV	BL-4-14	Quartz–barite vein	Quartz	−68	20.4	248	11.4	−3.6
VII	BL-7-5	Quartz vein	Quartz	−55	19.6	281	12	−3.3

Note: Quartz vein formed in siderite–quartz substage, other veins formed in quartz–barite–calcite substage. T_h average value of homogenization temperature of fluid inclusions in quartz.

Table 7
Comparative features of different types of gold deposits

Type	Deposit	Host rocks	Relation between orebody and wall rock	Wall-rock alteration	Main mineral assemblages	Gold ore type	Occurrence of barite	δ^{34}S(‰) of sulfide	δ^{34}S(‰) of barite	Source of sulfur	References
Quartz–barite vein type	Bulong Au deposit	Fine clastic rock	Generally concordant, locally cutting bedding	Silicification, pyritization, carbonation, sericitization	Quartz, barite, native gold, minor pyrite and carbonate	Quartz–barite vein and quartz vein	Vein	14.6–19.2	35.0–39.6	Strata, associated with reduction of sulfate	This paper
Sedex	Barite deposit in Xinhuang, Gongxi–Tianzhu, Dahebian	Siliceous rock and carbonaceous shale with phosphorite	Concordant		Barite (98%), calcite, pyrite, sericite, muscovite, organic matter		Stratified, local lenticular	14.6–24.2	32.3–41.6	Sea water, associated with organic matter and biological activities	Wang and Li, 1991; Che, 1995; Wu et al., 1999
	Jingtieshan Fe deposit, Gansu province	Phyllite, quartzite	Concordant		Specularite, siderite, pyrite, chalcopyrite, barite, carbonate		Stratified, banded and lenticular	8.1–15.6	19.7–33.6	Sulfate from sea water	Mao et al., 2003b
VMS	Gacun Au–Cu polymetallic deposit, Sichuan Province	Mafic volcanic rock, felsic volcanic rock	Concordant	Silicification, sericitization, chloritization, epidotization, kaolinite, calcitization	Pyrite, sphalerite, galena, chalcopyrite, barite, quartz, jasper	Associated gold	Stratified and banded	−4.6 to 3.1	13.8–22.5	Volcanic activity and seawater	Yu et al., 2000; Chen et al., 2001
	Hellyer volcanic-hosted massive sulfide deposit (Australia)	Mafic to felsic volcanic and volcaniclastics	Concordant	Silicification, chloritization, albitization, sericitization, epidotization	Pyrite, chalcopyrite, sphalerite, galena, arsenopyrite, tetrahedrite, quartz, barite, calcite, chlorite, sericite, siderite	Associated gold	Stratified	−18 to 40, main 6–12	32.4 to 49.5 with a peak around 43	Partially reduced seawater sulfate, igneous sulfur, life sulfate	Gemmell and Fulton, 2001
Carlin-type gold deposit	Laerma Au deposit, Gansu province	Carbonaceous sericite slate, carbonaceous siliceous slate	Generally concordant	Silicification, sericitization, stibnitization, barite, dickite, carbonation	Native gold, pyrite, stibnite, chalcopyrite, cinnabar, quartz, barite dickite	Siliceous rock type, slate type and dacite porphyry type	Disseminated (gold-bearing), vein (late mineralization stage)	−32.3 to −25.2; 1.6–21.5	2.4–28.5	Sedimentary sulfur in siliceous formation	Yao, 1994; Liu et al., 2000; Mao et al., 2002c
	Carlin-type Au deposit of the Nevada (USA)	Marine carbonate rock and fine clastic rock	Discordant	Silicification–jasperoidization, pyritization, carbonation, arsenopyritization, baritization, realgar, arsenopyritization, orpiment	Pyrite, orpiment, realgar, stibnite, cinnabar, chalcopyrite, native gold, kaolinite, barite	Normal type, siliceous type, pyrite type, carbonaceous type and arsenic-rich type	Vein, formed in late mineralization stage	−13.8 to 16.5	Early barite: 25.9–47.1; late barite: 14.5–39.4	Multiple sources	Arehart, 1996; Emsbo et al., 1999; Emsbo and Hofstra, 2003; Yigit et al., 2003; Nutt and Hofstra, 2003; Kesler et al., 2003a

Orogenic gold deposit	Orogenic gold deposits of the Yilgarn Block; Muruntau; Ashanti (Ghana), Mother lode (USA)	Metamorphic rock, main greenschist-facies host rocks	Discordant	Carbonation, pyritization, arsenopyritization, sericitization, K-feldspar, biotitization, chloritization	Mainly Fe-sulfides, arsenopyrite, pyrite, pyrrhotite	Gold-bearing quartz vein, stockwork	Barren barite-rich	<10	Deep source	Groves et al., 1998, 2000; Goldfarb et al., 2001
Low-sulfidation epithermal gold deposit	Axi Au deposit, Xinjiang in China	Pyroclastic rock, lava	Discordant	Sericitization, adularization, silicification, chloritization, propylitization, argillization	Pyrite, marcasite, arsenopyrite, sphalerite, adularia, quartz, few barite	Quartz vein, altered rock, breccia	Disseminated	0.9–10.2	Deep or magma source	Chen et al., 2001; Jia et al., 2001; Jiang and Wang, 2002
	Apacheta gold–silver deposit in Peru	Calc-alkaline lava flows and volcanic breccias	Discordant	Sericitization, adularization	Pyrite, tennantite, sphalerite, galena, chalcopyrite, electrum, acanthite, calcite, quartz, adularia	Vein type	No			André-Mayer et al., 2002
High-sulfidation epithermal gold deposit	Veladero gold deposit (Argentina), Yanacocha Au–Ag deposit (Peru), Pueblo Viejo gold deposit (Dominican Republic)	Volcanic and volcaniclastic rocks	Discordant	Silicification, alunitization, chloritization, kaolinization, pyrophyllite	Pyrite, chalcopyrite, tennantite, native gold, quartz, barite, kaolinite, alunite, pyrophyllite, alunite	Vein type, disseminated	Vein		Magma source	Corbett, 2002; Kesler et al., 2003b
	Zijinshan Cu–Au deposit, Fujian province	Dacitic porphyrite, breccia	Discordant	Silicification, dickite, alunitization, sericitization and pyritization	Pyrite, native gold, chalcopyrite, digenite, quartz, dickite, barite	Oxidized ore	Veinlet filling in fracture	−8.4 to 6.9	Mantle source	Zhang et al., 1991, 2003

sions in quartz in the same stage of the same sample, the $\delta^{18}O_{fluid}$ values of the mineralizing fluids are calculated to be 6.7‰ to 14.7‰, with a mean of 10.9‰. $\delta^{18}O_{fluid}$ values range from 8.6‰ to 14.7‰ with a mean of 11.8‰ for the siderite–quartz substage and from 6.7‰ to 11.4‰ with a mean of 9.8‰ for the quartz–barite–calcite substage. The δD values of fluids vary from −70‰ to −55‰ with a mean value of −63.4‰.

6. Discussion

6.1. Source of ore sulfur

The sulfur isotopic compositions of pyrite and barite are homogeneous and the $\delta^{34}S$ values have a narrow range, suggesting the sulfur in ore-forming fluids was derived from a single source. Both the presence of barite as well as the association of barite+pyrite within the ore assemblage imply that the deposit formed under conditions of high oxygen fugacity (Ohmoto, 1972; Zheng and Chen, 2000), but this is inconsistent with the considerable CH_4 content in carbonic inclusions. The CH_4 in carbonic inclusions is therefore interpreted as a result of post-entrapment modification of fluid inclusions. The possibility of fluid inclusion re-equilibration by diffusion of H_2 into the inclusions according to reactions such as $CO_2+4H_2=CH_4+2H_2O$ might explain this conflict on the redox state of ore fluids and fluid inclusion composition in carbonic inclusions (Hall and Sterner, 1995; Fan et al., 2003).

Sulfur isotope composition of total sulfur in a hydrothermal system where sulfide–sulfate fractionation is close to equilibrium ($\delta^{34}S_{barite-pyrite}$=~17‰ corresponding to T_{eq}~320 °C) should depend on the mass ratio of reduced and oxidized sulfur species between the two values (Seal et al., 2000). Thus $\delta^{34}S_{total}$ is located somewhere between +17‰ and +37‰, indicating that the total sulfur could have been derived from either Paleozoic seawater or sedimentary host rocks.

The $\delta^{34}S$ values of the Bulong gold deposit are all positive and characterized by enrichment in heavy sulfur. Elevated $\delta^{34}S$ values of barite are common in MVT deposits (Seal et al., 2000) and some Sedex barite deposits (Table 7). For example, $\delta^{34}S$ values of the Xinhuang, Gongxi–Tianzhu, and Dahebian barite deposits, located on the border between Hunan and Guizhou Provinces, reach 32.3–41.6‰ (Wang and Li, 1991; Che, 1995; Wu et al., 1999), and $\delta^{34}S$ values of the Vulcan barite deposit in Canada cluster about 43.5‰ (Mako and Shanks, 1984). Enrichment in heavy sulfur in sediment-hosted deposits has been attributed to sulfate-reducing bacteria (Wang and Li, 1991; Wu et al., 1999; Poole and Emsbo, 2000; Seal et al., 2000). According to these studies, sulfur in barite deposits originates from marine sulfate, with organic matter, bacteria and biological activities causing intense fractionation of sulfate ions, thus causing enrichment in $\delta^{34}S$. However, the Bulong gold deposit is an epigenetic, hydrothermal vein deposit and its age is distinctly younger than that of its host strata; because no marine environment existed, organic matter or bacteria are unlikely to have caused direct reduction of sulfate from seawater. Therefore, sulphides in the Bulong deposit are more likely to be the product of inorganic reduction of marine sulfate. In addition, the $\delta^{34}S$ values of barite are higher than those of its contemporary sulfate in seawater (~25‰, Zheng and Chen, 2000), suggesting that the sulfur underwent inorganic fractionation caused probably by hydrothermal activity.

6.2. Evolution of ore fluids

Fluid inclusions in the quartz stage are dominantly of H_2O–CO_2 ($\pm CH_4/N_2$)–NaCl type and are assumed to have been trapped during crystallization of the earliest quartz. The molar volume of the CO_2 phase was determined from T_{mCO2} and T_{hCO2} using the data of Fan et al. (2003). The molar volumes of three-phase CO_2-type fluid inclusions are 70 to 90 cm^3/mol, the admixture of CH_4 are 8 to 15 mol%. The abundance of CO_2-type inclusions in the Bulong gold deposit indicates that the ore fluids were characterized by a relatively high content of CO_2 and small amount of CH_4 or N_2. The high content of CO_2 suggests that the fluids were probably derived from a deep-seated (Kerrich et al., 2001). The presence of halite-bearing, aqueous carbonic inclusions (type V) might indicate local mixing of CO_2–$H_2O \pm CH_4$ fluids with H_2O–NaCl fluids due to reopening of older inclusions during later fracturing (Ni et al., 2003).

Densities of ore fluids during the main mineralization stage are slightly lower than those in the barite stage. The variability of phase volume ratios (0.05 to 0.90) in aqueous carbon inclusions (type III and IV) suggest that post-entrapment reequilibration occurred with H_2O loss.

NaCl–H_2O fluids of the late-stage are characterized by the absence of the CO_2 component and aqueous brines (with halite), medium temperatures, low salinities and medium densities. Salinities decrease markedly in the late stage, indicating that a meteoric water component increases in the fluids during the late stage.

Ore fluids in the Bulong gold deposit are characterized by medium temperature, low pressure (140–200 × 10^5 Pa, Zheng et al., 1996; Yang and Wu, 1999), low to moderately high salinity and medium-high density. These characteristics are distinct from those of fluids typically associated with epithermal gold deposits. For the latter, ore fluids typically show low-temperature and low-salinity features (mostly <5 wt.% NaCl equiv.; Cooke and Simmons, 2000). For example, homogenization temperatures of fluid inclusions from the Waihi epithermal Au–Ag-base metal deposit in New Zealand are 190 to 295 °C, and salinities are 0.2 to 4.5 wt.% NaCl equiv (Brathwaite and Faure, 2002), but some high-sulfidation epithermal deposits have salinities >5 wt.% NaCl equiv, as exemplified by the Palai–Islica Au–Cu deposit in Spain (Carrillo et al., 2003).

6.3. Source of ore fluids

Noble gas isotope analysis has been widely applied to studying the Earth's evolution, mantle degassing, tectonic settings, fluid migration, source of ore fluids (Dunai and Baur, 1995; Wang and Mao, 1996). The marked difference in isotopic compositions of noble gases in the crust and the mantle may be used as an important indication for tracing the source of ore-forming fluids (Sano and Wakita, 1985). Pyrite is known to be a suitable trap for noble gases (Burnard et al., 1999). The pyrites analyzed in this study were euhedral with no sign of subsequent modification; therefore, the fluid inclusions were probably related to mineralization. The influences of the isotopic fractionation and post-mineralization fluids caused by diffuse He and Ar loss from fluid inclusions on the He and Ar isotopic compositions of pyrite are insignificant. The effect of the epigenetic–radiogenic ^{4}He and ^{40}Ar produced by decay of U, Th and K in pyrite on the analytic results is negligible (Norman and Musgrave, 1994; Hu et al., 1999). As the samples for the study were taken from underground workings, the effect of cosmogenic ^{3}He can be ruled out (Simmons et al., 1987; Stuart et al., 1995). Thus the He and Ar isotopic compositions shown in Table 4 is taken to approximately represent the initial values of ore-forming fluids.

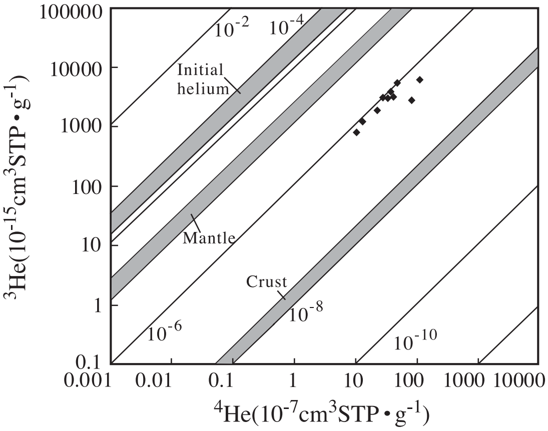

Fig. 12. Helium isotope composition of fluid inclusions in pyrite from the Bulong gold deposit (modified from Mamyrin and Tolstikhin, 1984). The data points of the Bulong gold deposit are close to the field of the crustal fluid component.

The ^{3}He/^{4}He ratios of fluid inclusions in pyrite are 0.24 to 0.82 (R/R_a), which are ten times higher than that of the crust (0.01 to 0.05 R/R_a; Stuart et al., 1995) but 10–30 times lower than that of the mantle (6 to 9 R/R_a). On a diagram of ^{3}He versus ^{4}He (Fig. 12), all of the data points of the helium isotope composition of fluid inclusions in pyrite plot between the crustal end-member and the mantle end-member. The percentage of mantle-derived He can be calculated according to the crust–mantle mixing model, which is expressed as:

$$\mathrm{He}_{\mathrm{mantle}}(\%) = \left\{\left({}^3\mathrm{He}/{}^4\mathrm{He}\right)_{\mathrm{sample}} - \left({}^3\mathrm{He}/{}^4\mathrm{He}\right)_{\mathrm{crust}}\right\} \Big/ \left\{\left({}^3\mathrm{He}/{}^4\mathrm{He}\right)_{\mathrm{mantle}} - \left({}^3\mathrm{He}/{}^4\mathrm{He}\right)_{\mathrm{crust}}\right\} \times 100 \text{ (Xu et al., 1996)},$$

where the lower limit of ^{3}He/^{4}He of the crust end-member is 2×10^{-8} and that of the mantle is 1.1×10^{-5} (Stuart et al., 1995). The calculation results show that the percentage of the mantle-derived He in the pyrite ranges from 2.8 to 10.3 (Table 4), averaging 7.4%. In general, ^{3}He/^{4}He ratios of ore fluids in the Bulong gold deposit are close to the crustal value, reflecting that the ore fluids mainly came from the crust and were possibly mixed with a minor amount of mantle component during the metallogenic process.

The helium isotope features of ore fluids in the Bulong gold deposit clearly differ from those of some other hydrothermal deposits in China, such as the Dashuigou tellurium deposit, Wangu Au deposit, Machangqing Cu deposit, Ailaoshan metallogenic belt, Jiaodong Au deposits and Dongping Au deposit, which are reported to have involved some mantle-derived fluids during mineralization. R/Ra values of ore-forming fluids in those deposits are generally 0.1 to 3.0 (Hu et al., 1997, 1999; Mao and Wei, 2000; Zhang et al., 2002) with elevated R/R_a values for the Dongping gold deposit ranging from 0.3 to 5.2 (Mao et al., 2003a); whereas the R/R_a values of ore-forming fluids of the Wangu gold deposit may reach up 3.5 to .8, illustrating that the dominant ore-forming fluids were derived from the mantle (Mao et al., 2002a).

The $^{40}Ar/^{36}Ar$ ratios of ore-forming fluids in the Bulong deposit are slightly higher than those of the atmosphere ($^{40}Ar/^{36}Ar = 295.5$), indicating the existence of a small amount of excess argon produced probably by higher radiogenic ^{40}Ar. The $^{40}Ar/^{4}He$ ratios of mantle fluids are 0.69 ± 0.006 and the average value of the crust is ~0.2 (Stuart et al., 1995). $^{40}Ar/^{4}He$ ratios of ore fluids in the Bulong gold deposit are similar to the value of the crust. The diagram of $^{3}He/^{4}He$ (R/R_a) vs. $^{40}Ar/^{36}$ of fluids in pyrite (Fig. 13) shows that the data points of the Bulong gold deposit are close to the field of the crustal fluid component, again indicating that the ore fluids were mainly derived from the crust.

The $\delta^{13}C_{PDB}$ values of fluid inclusions in quartz fall between magmatic carbon ($\delta^{13}C_{PDB} = -8‰$ to $-5‰$; Faure, 1986) and the field for marine carbonate ($\delta^{13}C_{PDB} = \pm 3‰$; Hoefs, 1997), but are closer to the latter and clearly different from those of organic carbon in sediments (average about $-25‰$, Clark et al., 2004), which possibly indicates that carbon in fluids from the Bulong deposit was mainly derived from marine carbonates.

The $\delta^{18}O$ values of the mineralizing fluids range from 6.7‰ to 14.7‰. Four samples analyzed fall in the range of magmatic water (5.5–9.5‰) defined by Ohmoto (1986) and Sheppard (1986). In a δD vs. $\delta^{18}O_{fluid}$ diagram (Fig. 14), four data points plot within or just adjacent to the magmatic water field and the other ten samples plot within the formation water below the metamorphic water, indicating that the ore fluids of the Bulong deposit were mainly derived from basinal fluids and mixed with a minor amount of magmatic fluids and meteoric water. This conclusion is consistent with the results from the He and Ar isotope analysis. From the siderite–quartz to the quartz–barite–calcite substage, the $\delta^{18}O_{SMOW}$ values decrease from 19.4‰ to 18.6‰ and the $\delta^{18}O$ values of the fluids decrease from 11.8‰ to 9.8‰. In the δD vs. $\delta^{18}O_{fluid}$ diagram (Fig. 13), the data points gradually shift toward the meteoric water line, implying the involvement of meteoric water in the ore-forming processes of the deposit and an increase of meteoric water towards the latter stages of mineralization.

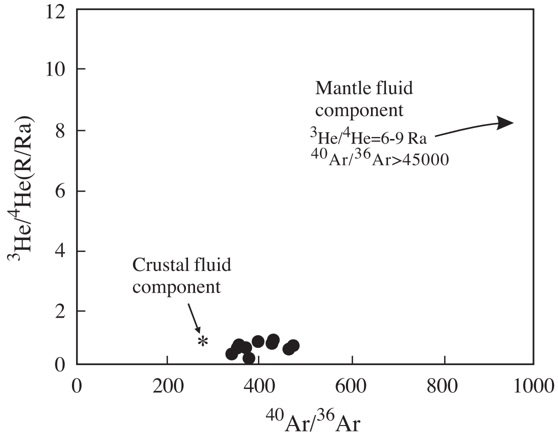

Fig. 13. Plot of $^{3}He/^{4}He$ (R/R_a) vs. $^{40}Ar/^{36}Ar$ ratios of the fluids in pyrite from the Bulong gold deposit. Pure meteoric or marine fluids are characterized by atmospheric He and Ar isotope compositions, therefore $^{3}He/^{4}He = 1.4 \times 10^{-6}$ and $^{40}Ar/^{36}Ar = 295.5$ are used to represent the pure crustal fluids. The ore fluids of the Bulong gold deposit reflect a dominant crust-derived source.

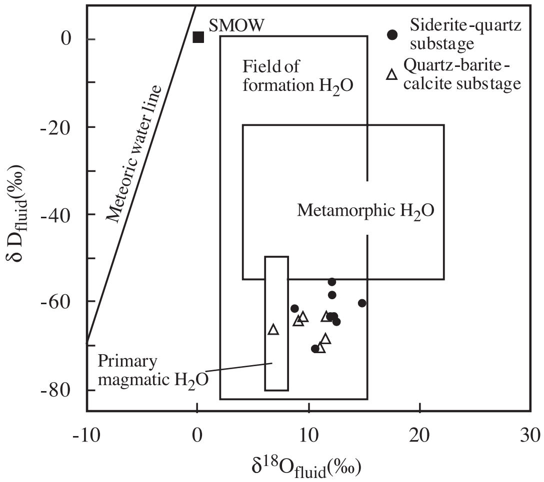

Fig. 14. δD–$\delta^{18}O_{fluid}$ diagram of the Bulong gold deposit (after Zheng and Chen, 2000).

6.4. Comparisons with other types of deposits

Barite deposits are mainly of sedimentary and hydrothermal type. The main characteristics of Sedex-type barite deposits are as follows (Table 7): orebodies are hosted in sedimentary rocks; the orebodies are stratified, concordant with the bedding of host strata; the ores have banded and laminated structures, showing typical sedimentary features. Barite is an important component in some Sedex-type lead–zinc deposits, such as the Tom deposit (Mao et al., 2003b). Barite in the Jingtieshan Sedex-type iron deposit is sufficiently enriched to be economic (Mao et al., 2003b). Barite in the above-mentioned deposits is generally stratified and massive–stratified, alternating with, or occurring inside or around sulphide (or specularite). Jasper interbeds commonly occur between barite beds and layered sulphide units (Mao et al., 2003b). In volcanic massive sulphide deposits (VMS), barite is generally well developed and occurs as stratified and massive units, alternating with massive to banded or laminated sulphide ores. Mineralization zonation is distinct in barite-bearing VMS deposits when compared to Sedex-type deposits (Lydon, 1984). Well-documented examples include the Kuroko deposits (Urabe and Marumo, 1992), and the Gacun deposit in China (Yu et al., 2000). Barite from the Bulong deposit has entirely different characteristics from the above-mentioned deposits (Table 7); both quartz–barite compound veins and large barite veins show no sedimentary features or zonation, and instead yield characteristics typical of epigenetic–hydrothermal vein-type deposits. Therefore, we consider it unlikely that the Bulong Au deposit is a modified Sedex or VMS deposit.

Carlin-type or sedimentary rock-hosted disseminated gold deposits are finely-disseminated, medium- to low-temperature hydrothermal gold deposits (John et al., 2003) that are hosted in fine clastic rocks, carbonate rocks and siliceous rocks which have not undergone regional metamorphism (Hofstra and Cline, 2000). A middle- to low-temperature, hydrothermal sulphide and alteration mineral assemblage comprising gold contained in arsenical pyrite, associated decalcification and sulfidation with variable silicification is commonly developed in such deposits. These assemblages form mainly at medium temperatures (~200 °C; John et al., 2003), low-salinity, H_2S-rich, Au-bearing fluids and gold grains are submicroscopic–microscopic (Romberger, 1986; Kuehn and Arthur, 1995; John et al., 2003). Barite is not universally developed in Carlin-type gold deposits and mostly occurs as veinlets or veins. The barite in these deposits, if present, forms late during mineralization (Ying, 2001) and is not closely related to gold mineralization, as exemplified by gold deposits in the Carlin trend, Gold Bar district and Alligator Ridge district of Nevada in the United States (Emsbo et al., 1999; Emsbo and Hofstra, 2003; Yigit et al., 2003), and the La'erma Au deposit in Gansu Province (Liu et al., 2000). In the Bulong deposit, host rocks are fine clastic rocks, orebodies comprise barite–quartz compound veins, the gold is closely associated with quartz and barite, the majority of gold occurs as micrograins, and visible gold is well developed. All these features indicate that the Bulong deposit does not belong to the Carlin-type of gold deposits.

Orogenic gold deposits represent a coherent group of widely distributed deposits in accretionary or collisional orogens of all ages. They form over an extended depth range (<5 to >15 km), although most commonly in greenschist-facies host rock, from a relatively uniform, deep source. In many terranes, first-order crustal-scale faults and shear zones control the regional distribution of the deposits (Groves et al., 1998, 2000; Goldfarb et al., 2001). Orogenic gold deposits, as exemplified by the gold deposits of the Yilgarn Block, Western Australia, and the Ashanti Au deposit, Ghana, are predominantly vein-hosted, low-sulphide and epigenetic, generally low-salinity (5 to 8 wt.% NaCl equiv), and not barite-rich (Groves et al., 1998, 2000). By contrast, orebodies in the Bulong deposit are barite–quartz compound veins and barite-rich, derived from relatively saline and low-CO_2 fluids (the main mineralization stage). These features differ from orogenic gold deposits.

Epithermal gold deposits are mainly hosted in igneous rocks that are closely related to porphyry systems (Hedenquist et al., 1998; Love et al., 1998; Muntean and Einaudi, 2001; Zhang et al., 2003), and their two end-members are low-sulphidation and high-sulphidation epithermal gold deposits. Low-sulphidation epithermal gold deposits, which are controlled by either calderas or composite faults/fracture system far away from the main calderas and commonly associated with regional Hg–Sb and Pb–Zn deposits, are characterised by the presence of large amounts of adularia, sericite and carbonate (Jiang and Wang, 2002), as exemplified by the Ladolam Au deposit in Papua New Guinea (Müller et al., 2002). High-sulphidation epithermal Au deposits are characterised by the formation of substantial amounts of alunite, kaolinite and other advanced argillic alteration (Berger and Henley, 1998) and are spatially closely associated with volcanic edifices, such as the Veladero Au deposit, Argentina (Corbett, 2002). In both low- and high-sulphidation epithermal Au deposits, small amounts of disseminated or veinlet barite can be common, as exemplified by the Axi Au deposit (Chen et al., 2001; Jiang and Wang, 2002), and the Zijinshan Cu–Au deposit (Zhang et al., 1991), both in China, but these barite occurrences are not necessarily related to Au mineralization. In the Bulong gold deposit and its surroundings, volcanic rocks and porphyry intrusion have not been recognised, and the main alteration indications for epithermal metallogenic systems such as alunite, kaolinite, adularia and K-feldspar are not recognised in altered wall rocks, either. In light of these differences, we therefore propose that the Bulong gold deposit is representative of an unusual quartz–barite vein type of gold deposit.

6.5. Conceptual model of the Bulong gold deposit

Zhao et al. (2002) reported a Rb–Sr isochron age of 258 ± 15 Ma from fluid inclusions in auriferous vein quartz of the Bulong gold deposit, implying that gold mineralization formed in the late Middle Permian. Uncertainties regarding the accuracy of this isochron age (due to possible fluid mixing) notwithstanding, this inferred mineralization age is similar to the age of the late mineralization stage of the Kanggu'er Au deposit in the East Tianshan (Rb–Sr isochron ages of 254 ± 7 to 258 ± 21 Ma on fluid inclusion in quartz; Li et al., 1998) and the ore-forming age of the Shiyingtan gold deposit (Rb–Sr isochron ages of 244 ± 7 to 288 ± 9 Ma; Feng et al., 2000). Many orogenic gold deposits elsewhere in the South Tianshan Mountains of Central Asia also formed in the Middle Permian, as exemplified by the Muruntau Au deposit (Rb–Sr isochron age of 256.2 ± 6.4 Ma determined on fluid inclusions in quartz from the second stage of mineralization; Kostitsyn, 1994), Daughyztau Au deposit (270–260 Ma; Yakubchuk et al., 2002), Amantaitau Au deposit (270–260 Ma; Yakubchuk et al., 2002), Zarmitang Au deposit (269 Ma; Yakubchuk et al., 2002), and the Kumtor Au deposit (284.4 ± 3.0 to 288.4 ± 0.6 Ma; Mao et al., 2004). These ages indicate that the late Hercynian epoch was the principal mineralization period for gold deposits in the South Tianshan Mountains of Central Asia and the Chinese Tianshan Mountains.

During the Early Permian, the Paleo-Tianshan Ocean eventually closed due to continent–continent collision of the Tarim plate and Ili–Issyk Lake microplate (Liu et al., 1996). Ductile shear zones, deep regional faults, thrust faults and thrust nappes formed during this collision. The compressional environment was transformed into the post-collisional extensional environment, resulting in widespread mantle uplift and crustal thinning. Continental volcanic eruptions occurred in the Kalpin area and the Southwest Tianshan, and Permian A-type granitoids (e.g., Huoshibulak granite) and diabase dikes intruded strata in the Southwestern Tianshan Mountains. Regional structures, magmatism and strong hydrothermal activity provided a favorable geodynamic setting for the formation of hydrothermal deposits.

The Bulong gold deposit is located near the regional Karateki fault, which separates the Late Paleozoic Southern Tianshan epicontinental basin from the Paleozoic Kalpin foreland basin. The first-order Karateki fault was active for extended periods of time and controls Late Hercynian granitoid intrusions, where well-developed secondary faults served as pathways and conduits for migration and accumulation of hydrothermal solutions. Two Hercynian sub-surface plutons occur in the northeast and southeast of the area (Wang, 2001), and several diabase dykes emplaced during the mineralization period also occur in the ore district, possibly providing thermal energy required for convective circulation of fluids. Our isotopical studies indicate that the sulfur and carbon derived from sedimentary host rocks or, in the case of sulfur, from evaporated seawater, and that the ore-forming fluid in the Bulong gold deposit was mainly derived from basinal fluids, possibly with some minor contributions from magmatic fluids and meteoric water. Therefore, the ore-forming processes in the Bulong gold deposit can be described as follows: Basinal fluids and possibly a minor amount of magmatic fluids and meteoric water migrated to generate the ore-forming system via convective circulation that was driven by magmatic heat. Hydrothermal ore solutions activated and extracted ore-forming materials such as gold and sulfur from the strata to form ore-forming hot brines. These ore-bearing hot brines migrated upwards along penetrating faults into near-surface interlayer fracture zones and second-order faults. Following a decrease in temperature and pressure, boiling, and water–rock exchange induced changes in the composition of ore fluids, and ore materials were precipitated from the solutions to form the quartz–barite vein type gold deposit.

7. Conclusion

The Bulong quartz–barite vein-type Au deposit in Xinjiang, northwestern China, located in the eastern part of the South Tien shan (or South Tianshan) world-class gold belt, is a rare example of epigenetic, barite-rich gold deposits. It is hosted in Upper Devonian fine-grained clastic rocks. Gold mineralization is controlled by a group of gently tilted fractured zones. Based on the mineral assemblage and crosscutting relationship of the veins, four mineralization stages are identified, these are: (1) an early quartz stage, (2) a barite vein stage, (3) a barite–quartz stage, and (4) a late-stage ankerite–calcite veinlet stage. Main stage gold mineralization is present in quartz–barite compound veins, although there are also abundant barren barite veins and large barren quartz veins in the ore district.

Homogenization temperatures of fluid inclusions from the Bulong gold deposit vary from 159 to 390 °C with a range of 200 to 340 °C for the main mineralization stage. Their corresponding salinity ranges from 2.4 to 46.2 wt.% NaCl equiv. with salinities for the main stage clustering between 7 and 18 wt.% NaCl equiv., and a peak of around 13 wt.% NaCl equiv. The densities of the fluid inclusions range from 0.73 to 1.13 g/cm^3.

The δ^{34}S values of pyrite and barite indicate that the sulfur was derived from the sedimentary host rock strata. Helium and Ar isotope compositions of fluid inclusions suggest that the ore fluids of the Bulong gold deposit were mainly derived from the crust and were mixed with a minor amount of mantle-derived (?magmatic) fluid component during the metallogenic process. Carbon, O and H isotopic data also imply that the ore-forming fluids were mainly derived from basinal fluids, with some minor involvement of possibly magmatic fluids and meteoric water. Changes in physico-chemical conditions and fluid compositions of the ore fluids during their ascent along faults and fracture networks played important roles in ore-forming processes of the Bulong gold deposit.

Acknowledgements

We are grateful to the No. 8 Geological Party of the Xinjiang Bureau of Geology and Mineral Exploration and Development, the Akqi Administration of Mineral Resource and the Bulong Gold Mine for their supports and help. Dr. Amantuer is thanked for his help during the fieldwork. Wang Lijuan is thanked for her assistance with the microthermometric measurements of fluid inclusions. This work was granted by the Major State Basic Research Program of the People's Republic of China (No. 2001CB 409807 and G 1999043216). This is also a contribution to the IGCP-473 project. Extensive and thorough reviews by A. Gilg, P. Neumayr and one anonymous reviewer helped to significantly improve the quality of the manuscript.

References

André-Mayer, A.S., Leroy, J.L., Bailly, L., Chauvet, A., Marcoux, E., Grancea, L., Liosa, F., Rosas, J., 2002. Boiling and vertical mineralization zoning: a case study from the Apacheta low-sulfidation epithermal gold–silver deposit, southern Peru. Mineralium Deposita 37, 452–464.

Arehart, G.B., 1996. Characteristics and origin of sediment-hosted disseminated gold deposits: a review. Ore Geology Review 16, 383–403.

Berger, B.R., Henley, R.W., 1998. Advances in the understanding of epithermal gold–silver deposits, with special reference to the Western United States. Economic Geology 91, 405–423.

Bodnar, R.J., 1992. The system H_2O–NaCl. PACROFIIV. Program and Abstracts, 108–111.

Bortnikov, N.S., Prokofev, V.Yu., Razdolina, N.V., 1996. Origin of the Charmitan gold–quartz deposit (Uzbekistan). Geology of Ore Deposits 38, 208–226.

Brathwaite, R., Faure, K., 2002. The Waihi epithermal gold–silver–base metal sulfide–quartz vein system, New Zealand: temperature and salinity controls on electrum and sulfide deposition. Economic Geology 97, 269–290.

Burnard, P.G., Hu, R., Turner, G., Bi, X.W., 1999. Mantle, crustal and atmospheric noble gases in Ailaoshan gold deposits, Yunnan Province, China. Geochimica et Cosmochimica Acta 63, 1595–1604.

Burruss, R.C., 1981. Analysis of phase equilibria in C–O–H–S fluid inclusions. In: Hollister, L.S., Crawford, M.L. (Eds.), Short Course Handbook. Mineralogical Association of Canada, vol. 6, pp. 39–74.

Cai, D.S., Lu, H.F., Jia, D., Wu, S.M., 1995. Paleozoic plate tectonic evolution of southern Tianshan. Geological Review 41, 432–442 (in Chinese with English abstract).

Carrillo, R.F.J., Morales, R.S., Boyce, A.J., 2003. High and intermediate sulphidation environment in the same hydrothermal deposit: the example of Au–Cu Palai–Islica deposit, Carboneras (Almeria). In: Eliopoulos, D.-G., et al. (Ed.), Mineral Deposits and Sustainable Development. Millpress, Rotterdam, Rotterdam, pp. 469–472.

Che, Q.J., 1995. A metallogenic model for sedimentary Gongxi-type barite deposits. Geotectonica et Metallogenia 19, 288–289 (in Chinese with English abstract).

Chen, Y.C., Li, Z.N., Mu, R.S., Shen, B.F., Zou, G.H., Li, H.Q., Wang, Q.M., Lin, W.W., Li, W.K., Liu, G.Q., Ou, Y.Z.Q., Meng, F.Y., Wang, D.H., Zhang, Z.C., Mao, D.B., Chen, F.W., Li, J.C., Li, J.J., 2001. The Gold Deposits and Metallogenic Regularity in China. Geological Publishing House, Beijing, pp. 102–258 (in Chinese).

Clark, S.H.B., Poole, F.G., Wang, Z., 2004. Comparison of some sediment-hosted, stratiform barite deposits in China, the United States, and India. Ore Geology Reviews 24, 85–101.

Clayton, R.N., Mayeda, T.K., 1963. The use of bromine pentafluoride in the extraction of oxygen from oxides and silicates for isotopic analysis. Geochimica et Cosmochimica Acta 27, 43–52.

Clayton, R.N., O'Neil, J.R., Mayeda, T.K., 1972. Oxygen isotope exchange between quartz and water. Journal of Geophysical Research 77, 3057–3067.

Cole, A., Wilkinson, J.J., Halls, C., Serenko, T.J., 2000. Geological characteristics, tectonic setting and preliminary interpretations of the Jilau gold–quartz vein deposit, Tajikistan. Mineralium Deposita 35, 600–618.

Coleman, M.L., Sheppard, T.J., Durham, J.J., Rouse, J.E., Moore, G.R., 1982. Reduction of water with zinc for hydrogen isotope analysis. Analytical Chemistry 54, 993–995.

Cooke, D.R., Simmons, S.F., 2000. Characteristics and genesis of epithermal gold deposit. Reviews in Economic Geology 23, 221–244.

Corbett, G., 2002. Epithermal gold for explorationists. AIG Journal — Applied Geoscientific Practice and Research in Australia April, 1–26.

Darling, S.D., 1991. An extended equation to calculate NaCl contents from final clathrate melting temperatures in H_2O–CO_2–NaCl fluid inclusions: implications for P–T isochore location. Geochimica et Cosmochimica Acta 55, 3869–3871.

Dunai, T.J., Baur, H., 1995. Helium, neon and argon systematics of the European subcontinental mantle: implications for its geochemical evolution. Geochimica et Cosmochimica Acta 59, 2767–2783.

Emsbo, P., Hofstra, A.H., 2003. Origin and significance of post-ore dissolution collapse breccias cemented with calcite and barite at the Meikle gold deposit, northern Carlin Trend, Nevada. Economic Geology 98, 1243–1352.

Emsbo, P., Hutchinson, R.W., Hofstra, A.H., Volk, J.A., Bettles, K.H., Baschuk, G.J., Johnson, C.A., 1999. Syngenetic Au on the Carlin trend: implications for Carlin-type deposits. Geology 27, 59–62.

Fan, H., Zhai, M., Xie, Y., 2003. Ore-forming fluids associated with granite-hosted gold mineralization at the Sanshandao deposit, Jiaodong gold province, China. Mineralium Deposita 38, 739–750.

Faure, G., 1986. Principles of Isotope Geology, 2nd edition. Wiley, New York. 589 pp.

Feng, C.Y., Xue, C.J., Jin, J.S., Zhang, L.C., 2000. Geochemistry of the Xitan epithermal gold deposit, east Tianshan Mountains. Mineral Deposits 19, 322–329 (in Chinese with English abstract).

Gao, J., Xiao, X.C., Tang, Y.Q., Zhao, M., Wang, J., 1995. Preliminary research on the tectonostratigraphy in the Southwestern Tianshan Mountains. Journal of Stratigraphy 19, 122–128 (in Chinese with English abstract).

Gemmell, J.B., Fulton, R., 2001. Geology, genesis and exploration implications of the footwall and hanging-wall alteration associated with the Hellyer volcanic-hosted massive sulfide deposit, Tasmania, Australia. Economic Geology 96, 1003–1035.

Goldfarb, R.J., Groves, D.I., Gardoll, S., 2001. Orogenic gold and geologic time: a global synthesis. Ore Geology Reviews 18, 1–75.

Graupner, T., Kempe, U., Spooner, E.T.C, Bray, C.J., Kremenetsky, A.A., Irmer, G., 2001. Microthermometric, Laser Raman spectroscopic, and volatile-ion chromatographic analysis of hydrothermal fluids in the Paleozoic Muruntau Au-bearing quartz vein ore field, Uzbekistan. Economic Geology 96, 1–23.

Groves, D.I., Goldfarb, R.J., Gebre-Mariam, M., Hagemann, S.G., Robert, F., 1998. Orogenic gold deposits: a proposed classification in the context of their crustal distribution and relationship to other gold deposit types. Ore Geology Reviews 13, 7–27.

Groves, D.I., Goldfarb, R.J., Knox-Robinson, C.M., Ojala, J., Gardoll, S., Yun, G.Y., Holyland, P., 2000. Late-Kinematic timing of orogenic gold deposits and significance for computer-based exploration techniques with emphasis on the Yilgarn Block, Western Australia. Ore Geology Reviews 17, 1–38.

Hall, D.L., Sterner, S.M., 1995. Experimental diffusion of hydrogen into synthetic fluid inclusions in quartz. Journal of Metamorphic Geology 13, 345–355.

Hedenquist, J.W., Lowenstern, J.B., 1994. The role of magma in the formation of hydrothermal ore deposits. Nature 370, 519–527.

Hedenquist, J.W., Arribas, A.J., Reynolds, T.J., 1998. Evolution of an intrusion-centered hydrothermal system: far southeast Lepanto porphyry and epithermal Cu–Au deposits, Philippines. Economic Geology 93, 373–404.

Hoefs, J., 1997. Stable Isotope Geochemistry, 3rd edition. Springer-Verlag, Berlin, pp. 1–250.

Hofstra, A.H., Cline, J.S., 2000. Characteristics and models for Carlin-type gold deposits. Reviews in Economic Geology 13, 163–220.

Hu, R.Z., Bi, X.W., Turner, G., Burnard, P.G., 1997. Helium and argon isotope systematics in pyrite fluid inclusions of Machangqing copper deposit. Science in China, Series D: Earth Sciences 27, 503–508 (in Chinese).

Hu, R.Z., Bi, X.W., Turner, G., Burnard, P.G., 1999. Helium and argon isotope of the ore-forming fluids in Ailaoshan metallogenic belt. Science in China, Series D: Earth Sciences 29, 321–330 (in Chinese).

Jia, B., Wu, R.S., Tian, C.L., Sha, D.M., 2001. The characters of the mineralization fluid of Axi gold deposit in Xinjiang. Gold Geology 7, 39–46 (in Chinese with English abstract).

Jiang, X.W., Wang, Y.J., 2002. Characteristics and genesis of the minerogenetic series of the Axi type gold deposits in the west Tianshan. Geology in China 29, 203–207 (in Chinese with English abstract).

John, D.A., Hofstra, A.H., Theodore, T.G., 2003. A special issue devoted to gold deposits in northern Nevada: Part 1. Regional studies and epithermal deposits. Preface. Economic Geology 98, 225–234.

Kerrich, R., Goldfarb, R., Groves, D., Garwin, S., Jia, Y., 2001. The characteristics, origins and geodynamic settings of supergiant gold metallogenic provinces. Science in China, Series D: Earth Sciences 43, 1–68 (supp).

Kesler, S.E., Fortuna, J., Ye, Z., Alt, J.C., Core, D.P., Zohar, P., Borhauer, J., Chryssoulis, S., 2003a. Evaluation of the role of sulfidation in deposition of gold, Screamer Section of the Betze–post Carlin-type deposit, Nevada. Economic Geology 98, 1137–1157.

Kesler, S.E., Russell, N., McCurdy, K., 2003b. Trace-metal content of the Pueblo Viejo precious-metal deposits and their relation to other high-sulfidation epithermal systems. Mineralium Deposita 38, 668–682.

Kostitsyn, Yn A., 1994. Rb–Sr isotope studies on the Muruntau deposit: mineralized metasomatites. Geochemistry International 31, 21–34.

Kotov, N.V., Poritskaya, L.G., 1992. The Muruntau gold deposit: its geologic structure, metasomatic mineral associations and origin. International Geology Review 34, 77–87.

Kuehn, C.A., Arthur, W.R., 1995. Carlin gold deposits, Nevada: origin in a deep zone of mixing between normally pressured and over-pressured fluids. Economic Geology 90, 17–26.

Li, H.Q., Xie, C.F., Chang, H.L., Cai, H., Zhu, J.P, Zhuo, S., 1998. Study on Metallogenetic Chronology of Nonferrous and Precious Metallic Ore Deposits in North Xinjiang, China. Geological Publishing House, Beijing, pp. 63–83 (in Chinese with English abstract).

Li, Y., Li, J., Song, H., Guo, L., 2002. Helium isotope studies of the mantle xenoliths and megacrysts from the Cenozoic basalts in the eastern China. Science in China, Series D: Earth Sciences 45, 174–183.

Liu, B., Shen, K., 1999. Thermodynamics of Fluid Inclusions. Geological Publishing House, Beijing. 290 pp. (in Chinese with English abstract).

Liu, B.P., Wang, Z.Q., Zhang, C.H., Ma, H.W., Zhou, H., Zhu, H.R., Gong, Y.M., Jia, W.M., 1996. Tectonic Framework and Evolution in Southwest Tianshan Mountains, China. Publishing House of China University of Geoscience, Wuhan, pp. 1–118 (in Chinese with English abstract).

Liu, J.J., Zheng, M.H., Liu, J.M., Zhou, D.A., 2000. Sulfur isotopic composition and its geological significance of the Cambrian gold deposits in western Qinling, China. Journal of Changchun University of Science and Technology 30, 150–156 (in Chinese with English abstract).

Liu, J.J., Li, E.D., Long, X.R., Zheng, M.H., Wang, J.Z., Sang, H.Q., 2004. The metallogenetic age of Dashankou gold deposit in Xinjiang, Southwestern Tianshan Mountains. Journal of Jilin University (Earth Science Edition) 34, 37–43 (in Chinese with English abstract).

Love, D.A., Clark, A.H., Hodgson, C.J., Mortensen, J.K., Archibald, D.A., Farrar, E., 1998. The timing of adularia–sericite-type mineralization and alunite–kaolinite-type alteration, Mount Skukum epithermal deposit, Yukon Territory, Canada: Ar–Ar and U–Pb geochronology. Economic Geology 93, 437–462.

Lydon, J.W., 1984. Volcanogenic massive sulfide deposits: Part I. A descriptive model. Geoscience Canada 11, 195–202.

Ma, L., 2002. Geological Atlas of China. Geological Publishing House, Beijing, pp. 342–343 (in Chinese).

Mako, D.A., Shanks, W.C., 1984. Stratiform sulfide and barite–fluorite mineralization of the Vulcan prospect, Northwest Territories: exhalation of basinal brines along a faulted continental margin. Canadian Journal of Earth Sciences 21, 78 – 91.

Mamyrin, B.A., Tolstikhin, I.N., 1984. Heliun Isotopes in Nature. Elsevier, Amsterdam. 273 pp.

Mao, J.W., Wei, J.X., 2000. Helium and argon isotopic components of fluid inclusions and tracing to the source of metallogenic fluids in the Dashuigou tellurium deposit of Sichuan Province. Acta Geoscientia Sinica 21, 58 – 61 (in Chinese with English abstract).

Mao, J.W., Kerrich, R., Li, H., Li, Y., 2002a. High ^{3}He/^{4}He ratios in the Wangu gold deposit, Hunan Province, China: implications for mantle fluids along the Tanlu deep fault zone. Geochemical Journal 36, 197 – 208.

Mao, J.W., Wang, Y., Ding, T., Chen, Y., Wei, J., Yin, J., 2002b. Dashuiguo tellurium deposit in Sichuan province, China: S, C, O, and H isotope data and their implications on hydrothermal mineralization. Resource Geology 52, 15 – 23.

Mao, J.W., Qiu, Y., Goldfarb, R.J, Zhang, Z., Garwin, S., Fengshou, R., 2002c. Geology, distribution, and classification of gold deposits in the western Qinling belt, central China. Mineralium Deposita 37, 352 – 377.

Mao, J.W., Li, Y., Goldfarb, R.J., He, Y., Zaw, K., 2003a. Fluid inclusion and noble gas studies of the Dongping gold deposit, Hebei province, China: a mantle connection for mineralization? Economic Geology 98, 517 – 534.

Mao, J.W., Zhang, Z.C., Yang, J.M., Zuo, G.C., Zhang, Z.H., Ye, D.J., Wang, Z.L., Ren, F.S, Zhang, Y.J, Peng, C., Liu, Y.Z., Jiang, M., 2003b. The Metallogenic Series and Prospecting Assessment of Copper, Gold, Iron and Tungsten Polymetallic Ore Deposits in the West Sector of the Northern Qilian Mountains. Geological Publishing House, Beijing, pp. 157 – 242 (in Chinese).

Mao, J.W., Konopelko, D., Seltmann, R., Lehmann, B., Wen, C., Wang, Y., Eklund, O., 2004. Post-collisional age of the Kumtor gold deposit and timing of Hercynian events in the Tien Shan, Kyrgyzstan. Economic Geology 99, 1771 – 1780.

Müller, D., Kaminski, K., Uhlig, S., Graupner, T., Herzig, P.M., Hunt, S., 2002. The transition from porphyry- to epithermal-style gold mineralization at Ladolam, Lihir Island, Papua New Guinea: a reconnaissance study. Mineralium Deposita 37, 61 – 74.

Muntean, J.L., Einaudi, M.T., 2001. Porphyry–epithermal transition, Maricunga belt, northern Chile. Economic Geology 96, 743 – 772.

Ni, P., Rankin, A.H., Zhou, J., 2003. Fluid inclusion studies on carbonatite dyke and associated quartzite in Bayan Obo, Inner Mongolia, China. Acta Petrologica Sinica 19, 297 – 306 (in Chinese with English abstract).

No. 8 Geological Party of the Xinjiang Bureau of Geology and Mineral Exploration and Development, 1995. Inspecting and appraising report of the Bulong gold deposit in Akqi County, Xinjiang. Unpublished report, pp. 1–58 (in Chinese).

No. 8 Geological Party of the Xinjiang Bureau of Geology and Mineral Exploration and Development, 1999. Geological reconnaissance survey report of the Bulong gold deposit in Akqi County, Xinjiang. Unpublished Report, pp. 1–53 (in Chinese).

Norman, D.I., Musgrave, J.A., 1994. N_2–He–Ar compositions in fluid inclusions: indicators of fluid source. Geochimica et Cosmochimica Acta 58, 1119 – 1132.

Nutt, C.J., Hofstra, A.H., 2003. Alligator Ridge District, east-central Nevada, Carlin-type gold mineralization at shallow depths. Economic Geology 98, 1225 – 1242.

Ohmoto, H., 1972. Systematics of sulfur and carbon isotopes in hydrothermal ore deposits. Economic Geology 67, 551 – 578.

Ohmoto, H., 1986. Stable isotope geochemistry of ore deposits. Reviews in Mineralogy 16, 491 – 559.

Poole, F.G., Emsbo, P., 2000. Physical, chemical, and isotopic characteristics of stratiform barite deposits in marine rocks of western North America. Geological Society of America Abstracts with Programs 32, A-50.

Robinson, B., Kusakabe, M., 1975. Quantitative preparation of sulphur dioxide for ^{34}S/^{32}S analyses from sulphides by combustion with cuprous oxide. Analytical Chemistry 47, 1179.

Romberger, S.B., 1986. Ore deposits 9, disseminated gold deposits. Geoscience Canada 13, 27 – 32.

Sano, Y., Wakita, H., 1985. Geographical distribution of ^{3}He/^{4}He in Japan: implications for tectonics and incipient magmatism. Journal of Geophysical Research 90, 8729 – 8741.

Seal II, R.R., Alpers, C.N., Rye, R.O, 2000. Stable isotope systematics of sulfate minerals. In: Alpers, C.N., Jambor, J.L., Nordstrom, D.K. (Eds.), Sulfate Minerals: Crystallography, Geochemistry, and Environmental Significance. Reviews in Mineralogy and Geochemistry, vol. 40, pp. 541 – 593.

Sheppard, S.M.F., 1986. Characterization and isotopic variations in natural waters. Reviews in Mineralogy 16, 165 – 183.

Shu, L., Wang, B., Yang, F., Lu, H., Charvet, J., Laurent-Charvet, S., 2003. Polyphase tectonic events and Cenozoic basin-range coupling in the Tianshan belt, northwestern China. Acta Geologica Sinica 77, 457 – 467.

Simmons, S.F., Sawkins, F.J., Schlutter, D.J., 1987. Mantle-derived helium in two Peruvian hydrothermal ore deposits. Nature 329, 429 – 432.

Stuart, F.M., Burnard, P.G., Taylor, R.P., Turne, G., 1995. Resolving mantle and crustal contribution to ancient hydrothermal fluids: He–Ar isotopes in fluid inclusions from Dae Hwa W–Mo mineralisation, South Korea. Geochimica et Cosmochimica Acta 59, 4663 – 4673.

Urabe, T., Marumo, K., 1992. A new model for Kuroko-type deposits of Japan. Episodes 14, 246 – 251.

Wang, W.P., 2001. Characteristics of aeromagnetic field and metallogenic prognosis of Wuqia–Keping area, southwestern part of Tianshan. Uranium Geology 17, 162 – 167 (in Chinese with English abstract).

Wang, Z., Li, G., 1991. Barite and witherite deposits in Lower Cambrian shales of south China: stratigraphic distribution and geochemical characterization. Economic Geology 86, 354 – 363.

Wang, D.H, Mao, J.W., 1996. Advances in the studies of helium isotopes geology. Geological Science and Technology Information 15, 51 – 56 (in Chinese with English abstract).

Wilde, A.R., Layer, P., Mernagh, T., Foster, J., 2001. The giant Muruntau gold deposit: geologic, geochronologic, and fluid inclusion constraints on ore genesis. Economic Geology 96, 633 – 644.

Wu, C.D., Yang, C.Y., Chen, Q.Y., 1999. The hydrothermal sedimentary genesis of barite deposits in west Hunan and east Guizhou. Acta Scientiarum Naturalium Universitatis Pekinensis 35, 774 – 785 (in Chinese with English abstract).

Xinjiang Bureau of Geology and Mineral Exploration and Development, 1993. Regional Geology of XinJiang Uygur Autonomous Region. Geological Publishing House, Beijing. 408 pp. (in Chinese).

Xu, Y.C., Shen, P., Tao, M.X., Liu, W.H., 1996. Geochemistry of mantle-derived volatile in the natural gases of eastern petroleum and gas fields: I. New type of helium resources: industrial accumulation of mantle-derived helium in the sedimentary strata. Science in China, Series D: Earth Sciences 26, 1 – 8 (in Chinese).

Yakubchuk, A., Cole, A., Seltmann, R., Shatov, V., 2002. Tectonic setting, characteristics, and regional exploration criteria for gold mineralization in the Altaid orogenic collage: the Tien Shan Province as a key example. Society of Economic Geologists, Special Publication 9, 177–201.

Yang, F.Q., Wu, H., 1999. Geological characteristics and genesis of Bulong gold deposit in Xinjiang. Bulletin of the 562 Comprehensive Geological Party, Chinese Academy of Geological Science, vol. 14, pp. 60–68 (in Chinese with English abstract).

Yang, F.Q., Ye, Q.T., Fu, X.J., Ye, J.H., 1999. Distribution and metallogenic conditions of gold deposits in southwest Tianshan Mountains. Xinjiang Geology 17, 129–136 (in Chinese with English abstract).

Yang, F.Q., Wang, L.B., Ye, J.H., Fu, X.J., Li, H.M., 2001. Zircon U–Pb ages of granites in the Huoshi Bulak area, Xinjiang. Regional Geology of China 20, 267–273 (in Chinese with English abstract).

Yao, Z.Y., 1994. A preliminary discussion on geological characteristics and genesis of the Laerma gold deposit in Luqu county, Gansu province. Mineral Deposits 13, 19–27 (in Chinese with English abstract).

Ye, Q.T., Wu, Y.P., Fu, X.J., Chen, M.Y., Ye, J.H., Zhuang, D.Z., Yang, F.Q., Bai, H.H., 1999. Ore-Forming Conditions and Metallogenic Prognosis of Gold and Nonferrous Metallic Resources in Southwestern Tianshan Mountain. Geological Publishing House, Beijing, pp. 70–93 (in Chinese with English abstract).

Yigit, O., Nelson, E.P., Hitzman, M.W., Hofstra, A.H., 2003. Structural controls on Carlin-type gold mineralization in the Gold Bar District, Eureka County, Nevada. Economic Geology 98, 1173–1188.

Ying, H.L., 2001. Characteristics and origin of the Carlin-type gold deposits. Geology–Geochemistry 29, 56–64 (in Chinese with English abstract).

Yu, J.J., Hou, Z.Q., Qu, X.M., 2000. Origin of high ^{18}O ore forming fluids in Gacun Kuroko deposit. Acta Petrologica et Mineralogica 19, 382–389 (in Chinese with English abstract).

Zhang, D.Q., Li, D.X., Zhao, Y.M., Chen, J.H., Li, Z.L., Zhang, K.Y., 1991. The Zijinshan deposit: the first example of quartz–alunite type epithermal deposits in the continent of China. Geological Review 37, 481–491 (in Chinese with English abstract).

Zhang, L.C., Shen, Y.C., Li, H.M, Zeng, Q.D., Li, G.M., Liu, T.B., 2002. Helium and argon isotopic compositions of fluid inclusions and tracing to the source of ore-forming fluids for Jiaodong gold deposits. Acta Petrologica Sinica 18, 559–565 (in Chinese with English abstract).

Zhang, D.Q., She, H.Q., Li, D.X., Feng, C.Y., 2003. The porphyry-epithermal metallogenic system in the Zijinshan region, Fujian province. Acta Geologica Sinica 77, 253–261 (in Chinese with English abstract).

Zhao, R.F., Yang, J.G., Wang, M.C., Yao, W.G., 2002. The study of metallogenic geologic setting and prospecting potential evaluation in Southwestern Tianshan Mountains. Northwestern Geology 35, 101–121 (in Chinese with English abstract).

Zheng, Y.F., Chen, J.F., 2000. Stable Isotope Geochemistry. Science Press, Beijing, pp. 218–247 (in Chinese).

Zheng, M.H., Liu, J.J., Long, X.R., 1996. Ore-forming geological conditions and target study of Muruntau-type gold deposit in southern Tianshan Mountains. Xinjiang. Unpublished Report, pp. 29–42 (in Chinese).

Zheng, M.H., Zhang, S.T., Liu, J.J., Long, X.R., Song, X.Y., 2001. Geological Background and Metallogenic Mechanism of the Muruntau-Type Gold Deposits in Southwestern Tianshan Mountain. Geological Publishing House, Beijing, pp. 1–131 (in Chinese).

Zhu, H.P., Wang, L.J., Liu, J.M., 2003. Determination of quadrupole mass spectrometer for gaseous composition of fluid inclusion from different mineralization stages. Acta Petrologica Sinica 19, 314–318 (in Chinese with English abstract).